OXFORD JOURNAL
OF STUDENT
SCHOLARSHIP

Aircraft Wing Structural Design Optimization: A Machine-Learning and Finite-Element Validation Study

Aayush Pant
aayush.pant3129@gmail.com

ABSTRACT

Aircraft wing design requires balancing structural mass, aerodynamic efficiency, material selection, and practical operational constraints. This study investigates whether machine learning models developed from real, publicly documented aircraft data can yield useful and physically feasible guidance for aircraft wing structural design. A dataset of ten aircraft spanning many categories–including narrowbodies, widebodies, regional aircraft, cargo aircraft, and electric aircraft–was used to evaluate wing material composition, wing loading, and aspect ratio. Gaussian-process surrogates were fit to closed-form beam-theory, classical lamination, and drag models. These models then made use of constrained optimization in order to develop potential design improvements for the aircraft. However, because these surrogates reproduce analytical models, they are treated as optimization techniques rather than actual predictive models of measured data. The results showed that changing the material composition was the optimal change, as seven of the ten aircraft had composite material fractions in their wings that were below their aircraft category's target. The wing loading optimization produced nearly mass-neutral results, when using conservative constraints, whereas aspect ratio optimization was mostly limited by feasibility with regard to airport infrastructure rather than structural mass constraints. Independent CAD and finite-element analysis (FEA) was performed for five aircraft and three different materials each – Aluminum 7075-T6, a CFRP Baseline, and an ML-Optimized CFRP layup. After correcting a bonded-contact interface artifact and the cap-load directions, the FEA models were rebuilt. The peak von Mises stresses at the point-load and fixed-support locations revealed numerical singularities and were not used as validation. The 3.75x ratio between the ultimate and cruise peak stress values is just a check that the load cases were applied correctly. The section-average cap stress and tip deflection, which were the intended validation metrics, could not be obtained reliably from these models, so the FEA serves as a consistency check of the load cases, and does not validate the beam-theory sizing. Overall, the results demonstrate the potential of real-aircraft proxy models for preliminary wing design optimization while identifying opportunities for expanded datasets and higher-fidelity structural analysis.

INTRODUCTION

Around 2.5% of global CO_2 emissions result from aviation-related activities, and over 880 million metric tonnes of CO_2 were produced by aviation alone in 2023 (Ritchie, 2024). These values continue to increase each year at an alarming rate, with these metrics projected to double by 2050 (Climate Action Tracker, 2025). CO_2 emissions alone do not account for the total impact that aviation has on global warming, however, because non-CO_2 effects, like those from contrail cirrus formation and NO_x driven ozone and methane changes, contribute to around two-thirds of aviation's total radiative forcing. Radiative forcing is the difference between incoming energy and energy radiated back out into the environment, and aviation accounts for ~3.5% of effective radiative forcing. Some estimates attribute 4% of the global temperature rise since pre-industrial times to aviation (Ritchie, 2024).

Despite these alarming statistics, the aviation industry has made relatively limited progress towards addressing this issue. Aviation is well behind the curve when it comes to adopting measures to reduce its carbon footprint, and this is especially concerning with global demand for aviation projected to grow in the coming years (Ritchie, 2024). As a result, there is increasing pressure to shift towards low-carbon fuels or sustainable aviation fuel (SAF) at the very least, if not alternative energy sources like electric and hybrid aircraft, and improving energy efficiency (Climate Action Tracker, 2025).

Improving fuel efficiency has consequently become a major goal of the aviation industry, with the wing becoming a primary source of focus. The wing is simultaneously a source of lift and drag, and this tradeoff between the two has made it the most influential when it comes to maintaining or improving aircraft efficiency (Li et al., 2022; Barcenas et al., 2023). Several features of wings have been studied in this context: aspect ratio, which reflects the tradeoff between wing span and chord length, sweep angle, and the use of different materials like carbon-fiber-reinforced polymer (CFRP) instead of traditional aluminum alloys (Parveez et al., 2022). In certain modern designs such as the Boeing 787 and the Airbus A350, these materials constitute over half the total airframe weight, providing a greater strength-to-weight ratio than Aluminum (Parveez et al., 2022) and reducing corrosion in the Airbus A350 program (Airbus, 2025b).

More recent exploration has seen the emergence of all-electric or hybrid aircraft, such as NASA's X-57 Maxwell distributed-electric-propulsion demonstrator (NASA, 2026; Deere et al., 2017). However, current batteries have a lower energy density than jet fuel, which means they provide less energy per unit of mass (Pattanayak & Mavris, 2025). Consequently, these aircraft require particularly aggressive drag reduction strategies. This has been done by using much higher aspect ratios and near-zero sweep, because they also operate below the speed bracket where a swept wing would be favored (Deere et al., 2017).

Most recently machine learning optimization methods for aerospace design have become more readily available. These include gradient-boosted and deep-learning surrogate models that have been applied to benchmark geometries like NASA's Common Research Model (Li et al., 2022). Additionally, multi-fidelity deep-learning surrogate models have been applied to aerodynamic design optimization (Tao & Sun, 2019). These models have allowed for engineers to experiment with wing design options in a far

less costly manner (Le Clainche et al., 2023), however, these methods are mostly trained on simulated data which limits their usage. This poses a specific question for this study: can regression and optimization models built from real, publicly documented aircraft data produce wing design recommendations that are defensible through both statistical and structural analysis? To answer this, this study has three major objectives. Firstly, build proxy models (regressions on the dataset and surrogate-assisted optimization of analytical models) of wing material composition, wing loading, and wing aspect ratio based on a dataset created from publicly documented aircraft data. Secondly, use those models to generate design recommendations for at least one representative aircraft for each type. Finally, independently check those recommendations using CAD and finite element analysis, identifying where the two approaches agree and where they don't.

METHODS

Currently, there is limited use of real aircraft specification data in machine-learning-based tools, possibly due to the aviation industry having few reliable sources to retrieve data from. Instead of making use of simulated training data or a benchmark geometry, this study builds a proxy model that makes use of ten real, publicly documented aircraft (see Table 1 for dataset sources). These aircraft range from narrowbody, widebody, regional, cargo, and electric aircraft. The Python model used to generate the design estimates is based on the data from this dataset. It makes use of leave-one-out cross-validation and literature-bounded heuristics in order to maintain precision and reliability despite a small sample size. While machine learning is being applied to aerodynamic and structural wing design more, it has rarely been put together with independent structural validation. This study bridges that gap by not only building a proxy model from real aircraft data, but also validating its recommendations using CAD and finite-element analysis.

Table 1
Aircraft Dataset Sources

Aircraft	**Category**	**Dataset Source**
Airbus A320-200	Narrowbody	Airbus (2024)
Boeing 737-800	Narrowbody	Boeing Commercial Airplanes (2025, October)
Boeing 707-320B	Narrowbody	Palt (n.d.)
Airbus A350-900	Widebody	Airbus (2025a)
Boeing 777-300ER	Widebody	Boeing Commercial Airplanes (2024, December)
ATR 72-600	Regional	ATR (2020)

Embraer E175	Regional	GlobalAir.com (n.d.)
Boeing 747-8F	Cargo	Boeing Commercial Airplanes (2026, January)
Eviation Alice	Electric	Eviation (n.d.)
NASA X-57 Maxwell (Mod IV)	Electric	NASA (2026)

Table 2
Aircraft Dataset Values Used in the Analysis

Aircraft	**MTOW (kg)**	**Wing area (m^2)**	**Span (m)**	**Aspect Ratio**	**Sweep**	**Wing loading (kg/m^2)**	**Composite fraction**
Airbus A320-200	78,000	122.6	35.8	10.45	25°	636	~10%
Boeing 737-800	79,015	125.0	35.79	10.25	25°	632	~3%
Boeing 777-300ER	351,530	436.8	64.8	9.61	31.6°	805	~12%
Airbus A350-900	280,000	442.0	64.75	9.49	31.9°	633	~53%
ATR 72-600	22,800	61.0	27.05	12.00	Straigh t	374	~5-10%
Embraer E175	40,370	72.7	26	9.30	~22-23 °	555	~8%
Boeing 747-8F	448,000	560.0	68.4	8.35	37.5°	800	~10%
Boeing 707-320B	151,000	283.0	44.42	6.97	35°	534	0%
NASA X-57 Maxwell (Mod IV)	1,360	6.2	9.64	14.94	0°	219	~100%
Eviation Alice	7,484	N/A	19.2	N/A	N/A	N/A	~95%

Note. Values are published specifications (sources in Table 1). Composite fractions are airframe-level percentages as defined by sources, so they are not directly comparable with wing-level targets used in the rule-based comparisons.

Optimization Methods

There were four modeling approaches applied to the three design levers that this study analyzes. For the general, cross-aircraft trend analysis, single-feature ordinary least squares linear regressions (wing loading and aspect ratio as functions of log(maximum takeoff weight)) were fit to the nine aircraft that had usable data. These regressions were then validated using leave-one-out cross-validation, and paired with a deterministic rule-based engine to evaluate each aircraft against its aircraft category's targets for composite material fraction, aspect ratio, wing-tip devices, sweep angle, and wing loading. For the material composition optimization, the possible composite ply-layups were evaluated using Classical Lamination Theory (Jones, 1999), and then fit a Gaussian Process surrogate (Rasmussen & Williams, 2006) to the Classical Lamination Theory evaluation data. From there, the most optimal layup for each aircraft was found using multi-start Sequential Least Squares Programming (SLSQP) (Kraft, 1988) over a softmax-reparameterized ply-fraction simplex. For the wing loading and aspect ratio optimization, 180 possible wing designs were generated for each aircraft type , and the resulting spar mass and cruise drag values of those wing designs became the training data for the Gaussian Process surrogates. The optimal point was then found using constrained Bayesian optimization through an Expected Improvement acquisition function (Jones et al., 1998), verified through Raymer's method (Raymer, 2018) to check for feasibility. However, because these optimization surrogates were fit to smooth calculations through closed-form functions instead of measured aircraft data, they have near-perfect cross-validated R^2 values, which showcases how a Gaussian Process can approximate a known analytical function with incredible accuracy. Due to the fact that they cannot provide predictive accuracy against new real-world observations, this study treats them as an optimization technique based on an analytical model and separate from the regression layer.

CAD and Finite Element Analysis Methodology

For the CAD modeling, a two-cap spar design was used, instead of a full three-dimensional stress field. This is because a wingbox in bending, to first order, behaves like an I-beam. This means that the upper and lower caps carry most of the axial bending stress, whereas the shear web just reacts shear. Therefore, focusing the analytical model solely on the two cap areas – which are separated by the wingbox height– captures the primary load path that determines the required material. A fully detailed stress field was not used because it could not be independently validated due to a lack of available data. This method of simplification, where the wingbox is idealized as spar-caps carrying axial bending stress, is a standard approach in aircraft structural analysis (Megson, 2021), and has been applied specifically to comparing aluminum and CFRP wingbox designs in prior work as well (Korba et al., 2024). The purpose is not to predict an exact stress distribution, but to correctly size the main load-carrying material for the design. Additionally, because every material and aircraft in this study made use of the same idealization, any error that the simplification causes is systematic across every comparison, which cancels out instead of favoring a specific material or aircraft. It is also important to note that this is the same physical model that the actual material composition optimizer used to determine the required spar cap area for each of the

layups discussed in the previous section. The CAD work that has been done is not comparing the ML sizing with a different, independent physics model, rather it is asking if that idealization works with a real three-dimensional solution. This addresses a different and more useful question than simply repeating the beam-theory analysis.

In order to do an independent structural check on the beam-theory sizing that has been used throughout this study, each of the tested aircraft's wing spar was modeled in CAD and analyzed with finite element analysis. Due to there being no public and dimensionally-verified CAD model of any of the chosen wingboxes, each was generated parametrically from the model's own outputs. The beam-theory sizing used throughout this study (cap force F = M/h, where M is the root bending moment and h is the root wingbox height, and required cap area $A = F/\sigma_{allow}$) gave the required sizing in order to produce the CAD model, where each spar in the two spar system was built with two caps and separated by the wingbox's derived height. This keeps the finite element analysis (FEA) model and the sizing methods it checks consistent with one another, so any differences between them are an actual check on the numerical solution. The FEA model is built from the same sizing, and agreement between the two quantities verifies that the numerical solution and the load application are correct. The sizing assumptions themselves are not verified from this, and the section-average cap stress and tip-deflection comparisons described below were the intended tests of them, but could not be obtained reliably.

FEA Model Setup and Corrections

Each wing was modeled as a cantilever and had its root face fully fixed as a constraint. The ultimate load case was derived from the FAR/CS 25.337 limit maneuvering load factor of 2.5g multiplied by the FAR/CS 25.303 safety factor of 1.5 (Limit Maneuvering Load Factors, 14 C.F.R. § 25.337; Factor of Safety, 14 C.F.R. § 25.303). This provided the two load cases: a 1g cruise case, and a 3.75g ultimate case. The aerodynamic load was reduced to a root bending moment M, and an equivalent transverse point force P at a load station that was measured from the root for each individual aircraft type. For the FEA, the moment was converted into a cap axial force F = M/h, before being applied as a compressive force on the upper spar of the two-spar design, and a tensile force on the lower cap. The force was applied on the cap face inboard of the load-station plane, not as a point load at the station. The A320-200 and 777-300ER models were solved directly using the cap force F, whereas the other models made use of the transverse force P applied the same way, and their stresses were then multiplied by F/P (11.52, 10.22, and 16.89 for the ATR 72-600, 747-8F, and X-57 models, respectively). This method of scaling is exact for a linear static model, which is why this is possible. The ultimate case that was allowable for Aluminum 7075-T6 was the yield strength that it has (503 MPa), and the CFRP layups were represented by an isotropic-equivalent modulus E_x instead of an orthotropic laminate model.

The first-pass FEA models returned peak stresses that were not physical, and three of the modeling artifacts were corrected before the results were reported here. First, the caps and the load-station seam were joined with bonded contacts, which created a stress singularity at the interface. Then, the bodies were combined into a single solid through the Combine/Join feature, which reduced the A320 Aluminum peak stress from 4,750 MPa in the original to 852.2 MPa in the first test. Secondly, the cap loads had to act as opposing compression/tension force pairs rather than working in the same direction like they were

before. Lastly, the load-station seam was recreated by splitting the face and offsetting a plane at the correct distance such that the actual component stayed intact, but the load could be placed in the proper location (A320: 7,230 mm; 777-300ER: 13,738 mm; ATR 72-600: 5,735 mm; 747-8F: 14,501 mm; X-57: 2,044 mm).

When the mesh was refined, the peak von Mises stress at a sharp, fully fixed root corner does not converge. This indicates that the peak values are mesh-dependent and not physical stresses (Megson, 2021). Fillets of various sizes ranging from 5-30 mm were tested in order to relieve the stress from the root corner, but it couldn't be resolved and the peak didn't converge. In the A320 aluminum ultimate case for example, the original sharp corner had a von Mises stress of 7,872 MPa, and then this increased to 10,277 MPa and 13,673 MPa for two fillet sizes in order of increasing size). Based on Saint-Venant's principle, the stress away from the load and the support is independent of the application of the load itself. The intended validation metrics were therefore the section-average cap stress, $\sigma = M/(h \times A)$, read away from the corner and load station and compared to the beam-theory target, and the cruise tip deflection compared to the beam-theory prediction. These could not be reliably obtained from the present models, so the FEA is used as a consistency check on the load cases. The ultimate-to-cruise peak stress ratio is reported only as a check to ensure that the loads were applied correctly, and is a property of any linear solver. A mesh-size study based on the A320 aluminum cruise case is reported in Table 6, although not repeated for the other aircraft. In this study, the peak von Mises stress fell as the mesh was refined, so element size relative to the 45 mm cap thickness also inflated the coarse-mesh values, and no result here is yet mesh-converged.

RESULTS

General Trend Analysis (Machine Learning)

Nine of the ten aircraft datasets used had usable wing-area data, but the Eviation Alice didn't, because its wing area was not publicly disclosed information, so it was excluded from the linear-regression-based numeric fit. A linear-regression module fits two single-feature linear regressions–for the aspect ratio and wing loading–as functions of the value of log(maximum takeoff weight). These models are then evaluated using leave-one-out cross-validation in order to get an error estimate for this sample size, as well as cross-referencing with accepted engineering limitations for five aircraft categories: narrowbody, widebody, regional, cargo, and electric. Then, a deterministic rule-based engine evaluates each aircraft against the standard values for their aircraft type before providing detailed recommendations for each aircraft. The criteria for this evaluation include: composite fraction, aspect ratio, wingtip-device presence, sweep angle, and wing loading.

The clearest results were with regard to wing material composition with seven out of the ten aircraft being below the composite fraction targeted by their category for a modern design, meaning that many aircraft are carrying greater structural wing weight than a more modern design, particularly in the older airframes. The 707-320B, an all-aluminum aircraft from the 1950s, contains 0% composite compared to the 15-20% narrowbody target (Caliendo, 2015), which would result in an estimated 15% reduction in wing structural weight under the rule of thumb described below (though the 707 is a retired design, so this is a

comparison making use of a hypothetical new design, not a retrofit). The 737-800 and 777-300ER have 3% and 12% composite, respectively, when the narrowbody target is between 15-20% and the widebody target is 50-55%. If the category targets were met, then these aircraft would have wing structural weight savings of 12% and 14%. These estimates use the following rule of thumb: savings (%) = min(20, (target_low - current) / target_high × 20), where the current and target values are composite fractions as percentages, and the 20% cap is an author assumption rather than the output of a structural model. The current fractions being used are airframe-level percentages (Table 2) whereas the targets are wing-level, so the comparison is approximate, especially for the 777-300ER (12% of structure by weight). Only the A350-900, X-57, and Alice match their category norms for composite material percentage, although the Alice does have predominantly composite wings. The wing loading, however, showed a wider spread that was more category-dependent. The regression trend showed that wing loading could rise from roughly 357 kg/m^2 for electric aircraft to as high as 758 kg/m^2 for cargo aircraft as a function of takeoff weight, with a mean absolute error of 84.4 kg/m^2, roughly 15% relative to a typical value of 578.3 kg/m^2. Six of the ten aircraft differed from their category wing loading by 9% or more, where the most prominent were the ATR 72-600, lying 20% below the regional aircraft norm, and the 707-320B, lying 18% below the narrowbody norm. These trend models achieved leave-one-out cross-validated R^2 values of 0.75 and 0.66 for wing loading and aspect ratio, respectively (sample size of 9 aircraft across the five categories). This means that the results should be taken as directional trends with meaningful uncertainty instead of precise predictive relationships, although with heavier aircraft the fit is significantly closer. Lastly, the aspect-ratio predictions were more compact with a mean absolute error of 1.13, roughly 11% compared to a typical aspect ratio of 9.96. The category recommendations for aspect ratio ranged from 8.25 for cargo aircraft to 13.28 for electric, although only the 707-320B seemed to require a significant aspect-ratio change. If the 707-320B changed from its current 7.0 to the narrowbody target of 9.0-10.5, it would lead to an estimated 23% reduction in induced drag. The remaining recommendations from the machine learning model like the use of wingtip devices and sweep angle had less impact, and changes to these would not lead to significant differences in aircraft performance, or have already been explored. The composite-fraction comparison, the weight-saving estimate, and the wingtip-device and sweep recommendations came from deterministic rules applied to published values rather than trained models. Only the two regressions are trained from data.

Material Composition Optimization

The material-composition model does not just use the rule-based composite-fraction check used elsewhere in this study. It determines what ply layups would actually reduce the mass of the wings without sacrificing stiffness, whilst still factoring in the existing wingbox shapes and loads. Each of the possible layups is assessed using Classical Lamination Theory. This allows the model to take the fiber orientation and thickness fraction for each ply in the layup and create the laminate stiffness matrices that are necessary. It then provides an extensional modulus E_x and an allowable stress for the entire layup. The lamina properties were: E_1 = 181 GPa, E_2 = 10.3 GPa, G_{12} = 7.17 GPa, and ν_{12} = 0.28 (Jones, 1999). The allowable stress was computed using a ply-fraction rule of 1,500 MPa for 0° plies, 300 MPa for ±45° plies, and 50 MPa for 90° plies weighted by ply fraction. This is a sizing proxy and not a first-ply-failure criterion, and the design variables are the thickness fractions of a balanced 0/+45/-45/90 laminate, so absolute ply thicknesses and stacking sequences were not optimized. The Gaussian Process surrogates

that acted as replacements for the Classical Lamination Theory calculations were validated by 5-fold cross-validation before being utilized in the optimizer itself. This revealed an R^2 value of ≈ 1 for both the effective modulus and strength surrogates, with the modulus surrogate having a mean absolute error of 0.028 GPa and the strength surrogate having a mean absolute error of 0.003 MPa. An R^2 of ≈ 1 is the expected value here because the surrogate interpolates a smooth, deterministic analytical function with 200 randomly sampled layups and no measurement noise. This means that it shows interpolation accuracy and not actual predictive accuracy for real aircraft. The layup design space itself is a simplex, meaning that the ply fractions must add up to one, and each fraction must be positive. Then, the optimizer transforms the constrained search into one that is unconstrained by re-parameterizing the design making use of a softmax and real-valued logits. Following this, the optimizer runs Sequential Least Squares Programming (SLSQP) using 20 random restarts for each aircraft. This helps the optimizer search more broadly, that way it has a better chance of determining the best composite ply layup instead of settling on a weaker one that is only locally optimal. When the resulting ply fractions are placed side-by-side with those of the representative CFRP layup in the report, it demonstrates how misleading it is to rely on just one reference. This is because when the model forces the composite laminate to have the same E_x value as the representative laminate, the predicted weight savings drop to 11-13% across the eight aircraft with complete wingbox geometry available for this optimization, because the representative point has a stiffness penalty of ~43% and if the materials are only compared by mass, then this gets hidden, despite impacting the savings in reality. The Eviation Alice was excluded due to not having public wing area data. The Embraer E175 has public wing-area data, but due to being an aluminum-primary regional jet, it was excluded in order to limit scope as the A320 and 737-800 were already similar.

The optimized layups are reported in Table 3. Across the five aircraft, the optimizer chose about 12-13% 0° plies, 33-42% ±45° plies, and 46-54% 90° plies. The layups were constrained to match the aluminum cap's stiffness because the optimizer's feasibility check is that the cruise tip deflection does not exceed that of the aluminum design. The ply-fraction allowable stress for these layups is low (~322-329 MPa), meaning that the required cap area is ~53-56% larger than aluminum. The spar mass is still ~11-13% lower because the density of the CFRP used is 1,600 kg/m^3 compared to 2,810 kg/m^3 for aluminum. The large 90° fraction is due to the stiffness-matching sizing proxy, and has not been verified against a laminate failure criterion (see Limitations). The frontiers in Figures 1-5 are sparse: each frontier point is an SLSQP optimum at 1.3, 1.15, 1.0, or 0.9 times the aluminum cruise tip deflection.

Table 3

Composite ML-optimized Layups, Properties, and Mass Relative to Aluminum 7075-T6

Layup	0° (%)	±45° (%)	90° (%)	E_x (GPa)	Allowable (MPa)	Cap area vs. Al	Spar mass vs. Al
Airbus A320-200	12.3	39.9	47.8	46.8	328.6	1.53	0.87
Boeing 777-300ER	11.9	42.4	45.7	46.8	328.6	1.53	0.87
ATR 72-600	12.1	41.4	46.5	46.9	328.8	1.53	0.87

Boeing 747-8F	12.6	38.1	49.3	46.7	327.7	1.53	0.87
NASA X-57 Maxwell (Mod IV)	13.0	33.2	53.8	45.9	322.1	1.56	0.89
Rep. CFRP Baseline (all)	–	–	–	65.0	650.0	0.77	0.44

Note. Layups come from the optimizer's files. Cap area and spar mass are relative to the Aluminum 7075-T6 design for the same aircraft. Spar mass counts both wings, caps, the root cap area, and the semispan (taper and web not included).

Figure 1

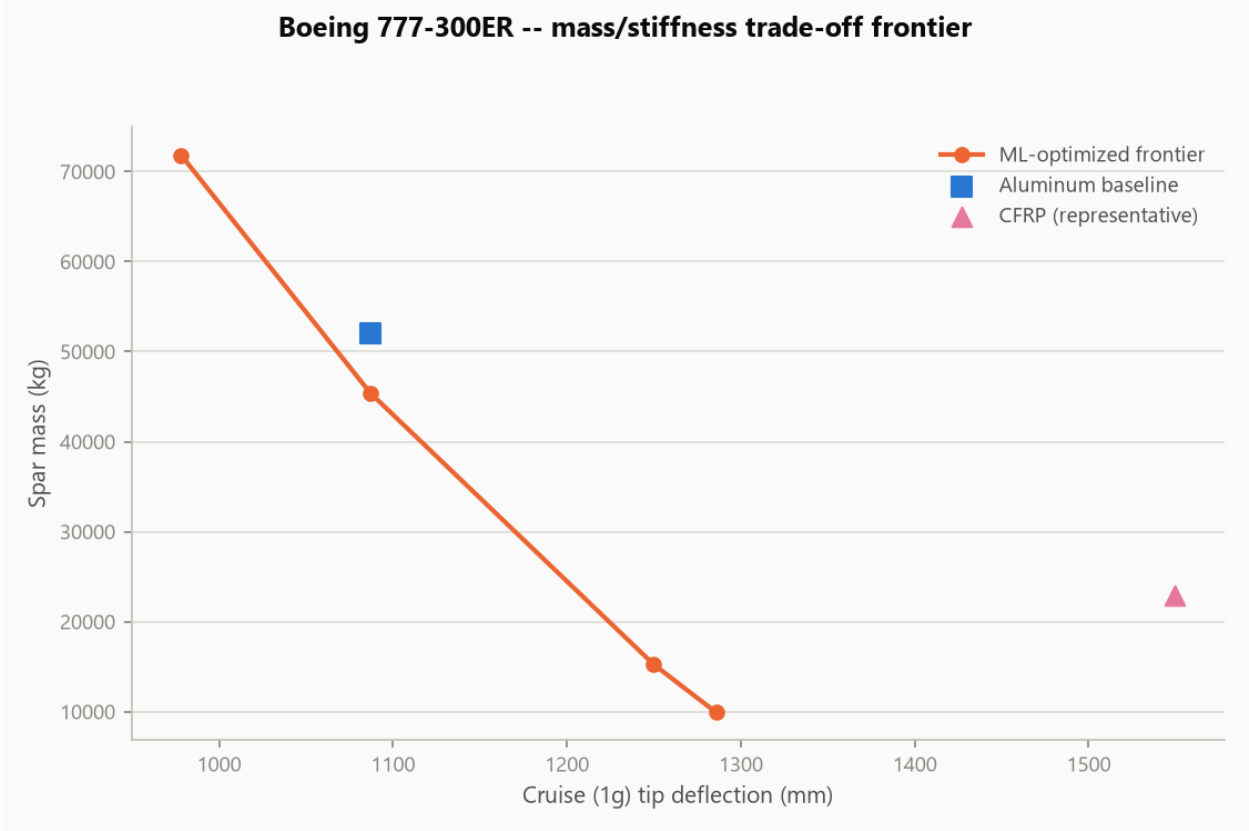
Airbus A320-200 Spar Mass-Stiffness Trade-off Frontier (CFRP Ply-Layup Optimization)



Note. Pareto frontier of CFRP ply-layup designs scored using Classical Lamination Theory, plotting spar mass (kg) against Cruise (1g) tip deflection (mm) for the A320-200. Each point on the ML-Optimized frontier is a different layup that was a part of the SLSQP optimization. For comparison, the Aluminum 7075-T6 and CFRP Baseline layups are plotted as well.

Figure 2

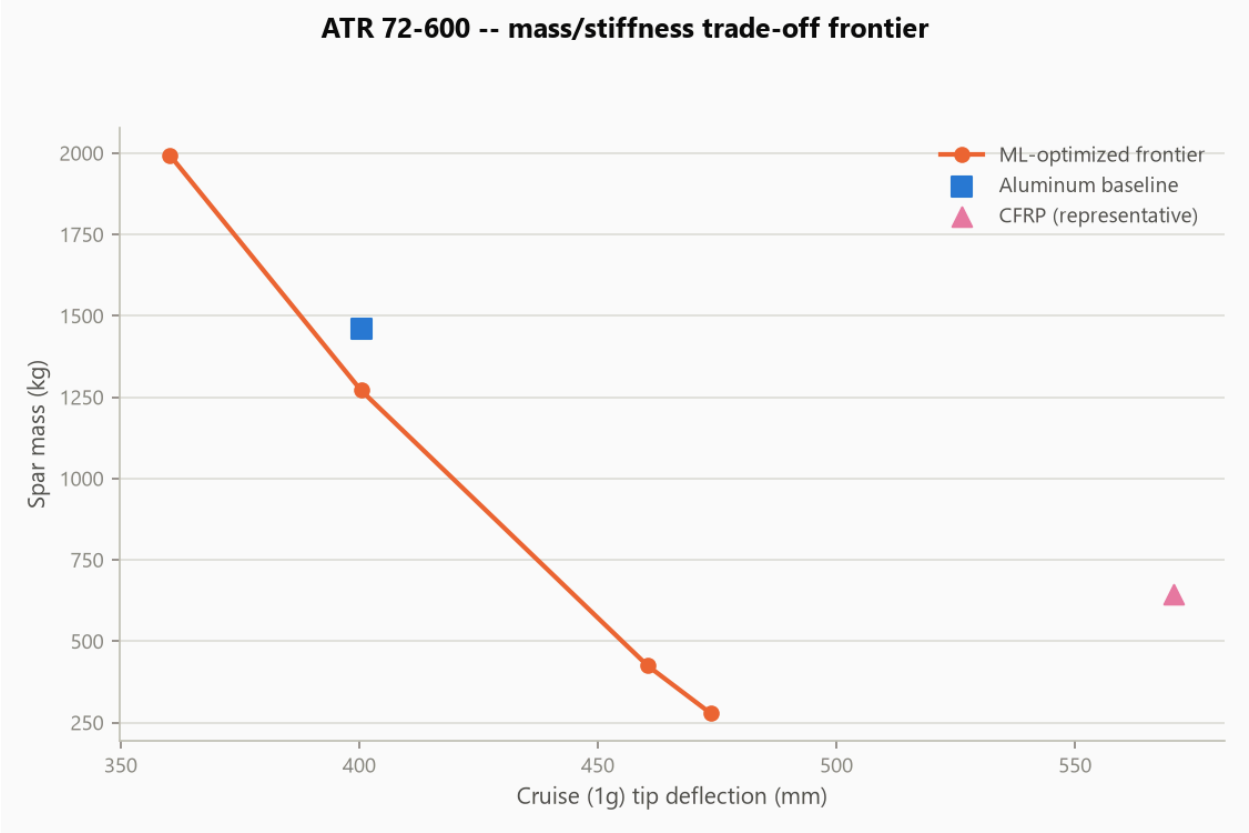
Boeing 777-300ER Spar Mass-Stiffness Trade-off Frontier (CFRP Ply-Layup Optimization)



Note. Pareto frontier of CFRP ply-layup designs scored using Classical Lamination Theory, plotting spar mass (kg) against Cruise (1g) tip deflection (mm) for the Boeing 777-300ER. Each point on the ML-Optimized frontier is a different layup that was a part of the SLSQP optimization. For comparison, the Aluminum 7075-T6 and CFRP Baseline layups are plotted as well.

Figure 3

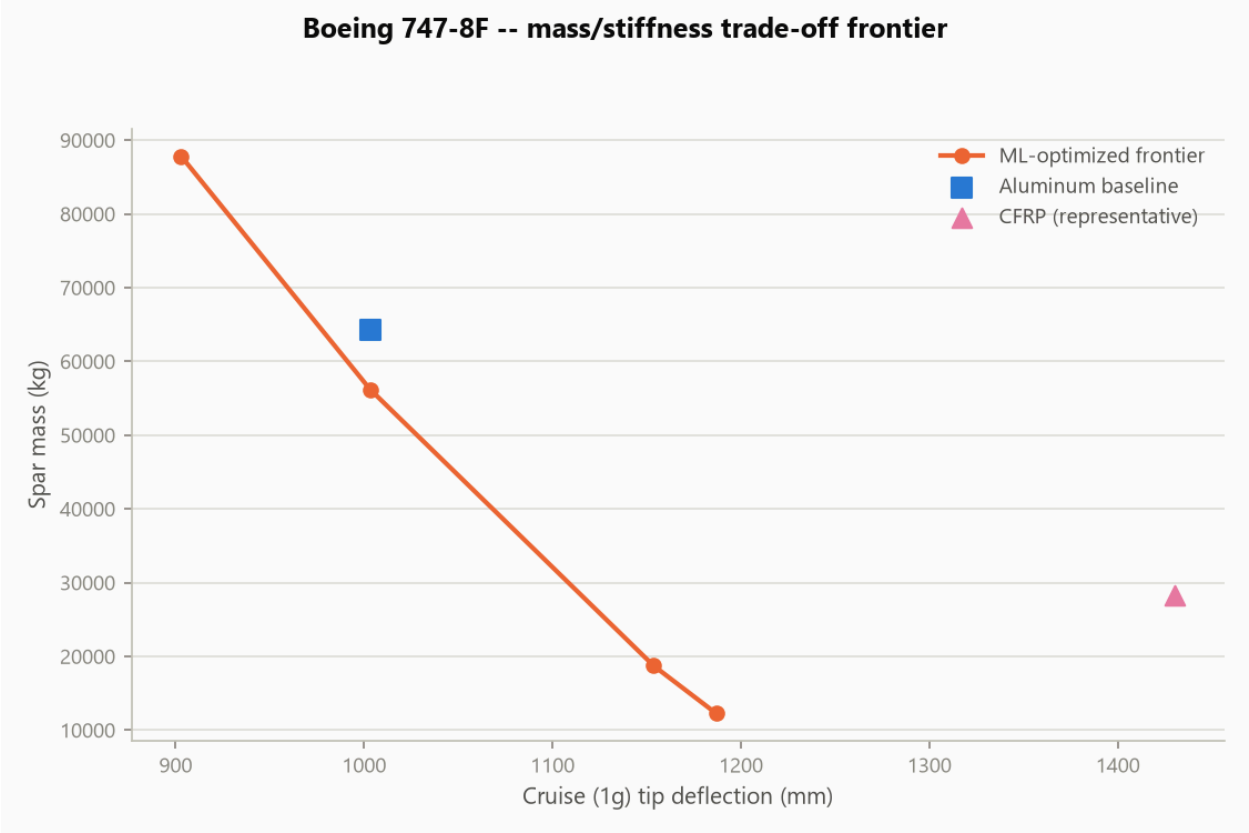
ATR 72-600 Spar Mass-Stiffness Trade-off Frontier (CFRP Ply-Layup Optimization)



Note. Pareto frontier of CFRP ply-layup designs scored using Classical Lamination Theory, plotting spar mass (kg) against Cruise (1g) tip deflection (mm) for the ATR 72-600. Each point on the ML-Optimized frontier is a different layup that was a part of the SLSQP optimization. For comparison, the Aluminum 7075-T6 and CFRP Baseline layups are plotted as well.

Figure 4

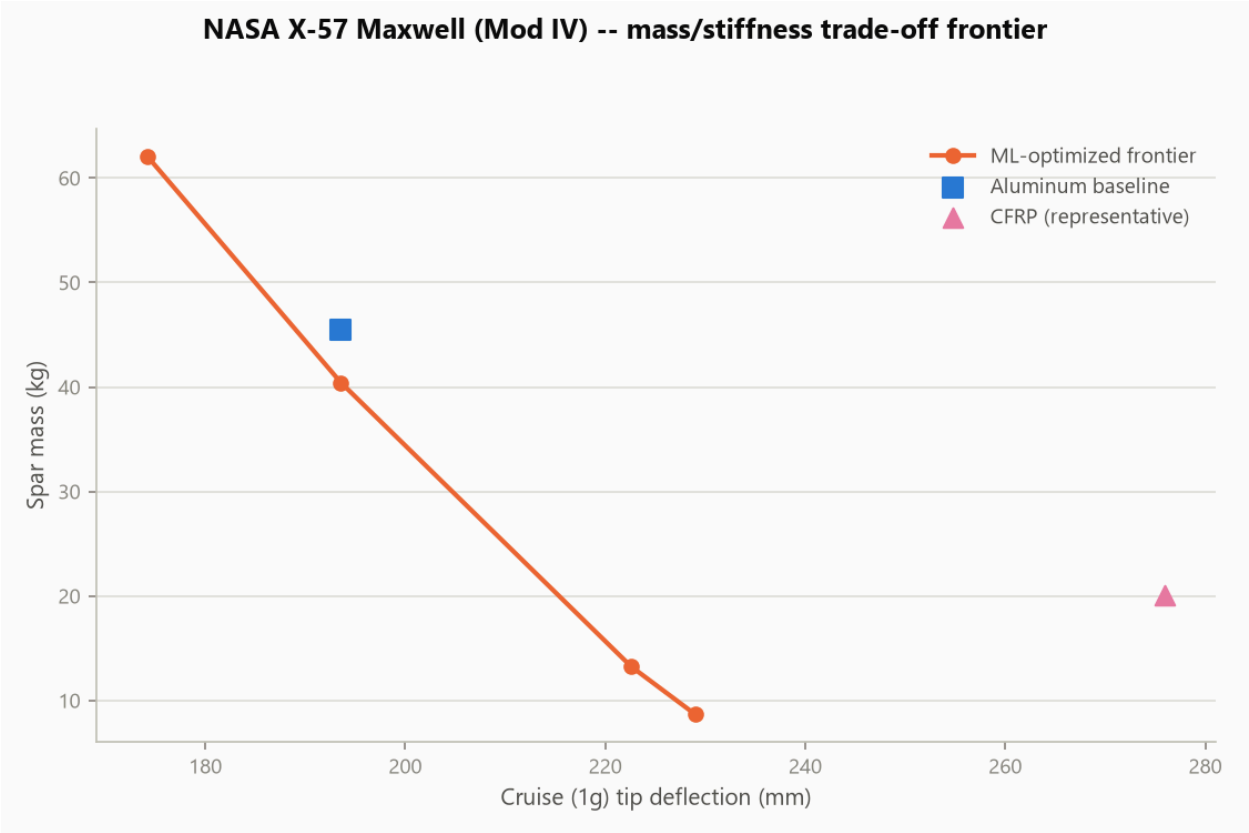
Boeing 747-8F Spar Mass-Stiffness Trade-off Frontier (CFRP Ply-Layup Optimization)



Note. Pareto frontier of CFRP ply-layup designs scored using Classical Lamination Theory, plotting spar mass (kg) against Cruise (1g) tip deflection (mm) for the Boeing 747-8F. Each point on the ML-Optimized frontier is a different layup that was a part of the SLSQP optimization. For comparison, the Aluminum 7075-T6 and CFRP Baseline layups are plotted as well.

Figure 5

NASA X-57 Maxwell Spar Mass-Stiffness Trade-off Frontier (CFRP Ply-Layup Optimization)



Note. Pareto frontier of CFRP ply-layup designs scored using Classical Lamination Theory, plotting spar mass (kg) against Cruise (1g) tip deflection (mm) for the NASA X-57 Maxwell. Each point on the ML-Optimized frontier is a different layup that was a part of the SLSQP optimization. For comparison, the Aluminum 7075-T6 and CFRP Baseline layups are plotted as well.

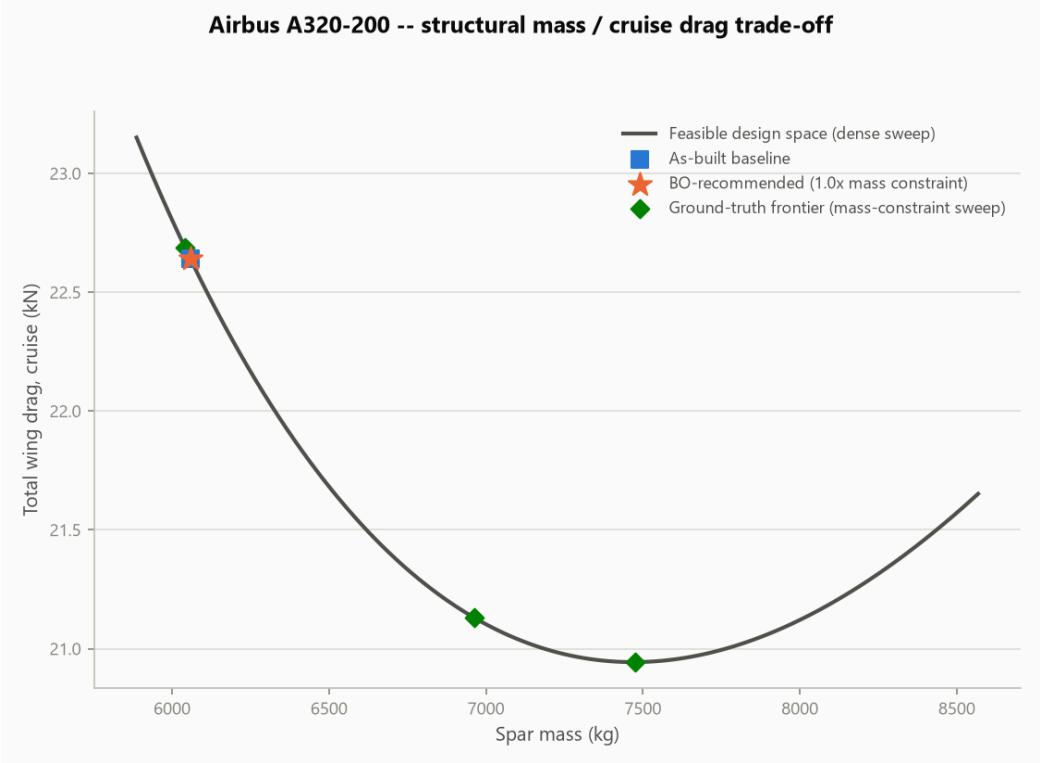
Wing Loading Optimization

The wing loading model treats the wing area as a continuous design variable with the aspect ratio being constant, making use of the formula $span_0 \times \sqrt{(S/S_0)}$ in order to scale the span of the wing. The model fits a Gaussian Process surrogate based on this formula, for both spar mass and cruise drag. Subsequently, it makes use of five-fold cross-validation in order to verify that the surrogate model is not overfitting and just memorizing the 180 wing-area design prototypes during training, rather than actually having a reasonable fit. Across the eight aircraft with complete wingbox geometry, the 5-fold cross-validated surrogate accuracy was extremely high. The R^2 values for spar mass and cruise drag were ≈ 1 in every case, and mean absolute error values ranging from 0.0-0.9 kg for spar mass and 0-3 N for cruise drag. Similar to the material composition model, this shows how the Gaussian Process replicates the

beam-theory and drag physics it was based on. Searching over the surrogate model makes use of constrained Bayesian optimization, and an Expected Improvement acquisition function determines the next candidate wing area to analyze. First, each possible wing area candidate goes through a feasibility check based on Raymer's approach, which ensures the optimizer does not recommend a wing area candidate that exceeds the maximum approach speed for that aircraft category (V_approach = 1.3 V-stall, evaluated at the landing weight with a category-specific landing $C_{L,max}$ and approach-speed ceiling). Making use of the most conservative constraint levels from the report, the optimizer's recommendation is nearly mass-neutral, suggesting a 0.14% reduction in spar mass for the wing. This appears modest, but increasing the mass budget to 1.3 times the current spar mass could reduce cruise drag by ~10.4%. At the drag minimum, the per-aircraft reductions were ~7.5% (A320-200), ~22% (777-300ER), ~16% (747-8F), ~4% (ATR 72-600) and ~10% (X-57). The mass versus drag curve between the two points is non-monotonic, which means that there is a genuine interior optimization instead of just one part being optimized. The near-zero result is the more reliable finding for this dataset, because it applies the strictest feasibility checks whereas the 1.3x-mass results are more of an upper limit on how much flexibility there is within the optimization before aircraft certification constraints become a major limitation. The spar mass here is defined as 2 wings × 2 caps × root cap area × semispan × material density, so this is a relative sizing metric and not the actual mass of a real wing structure.

Figure 6

Airbus A320-200 Structural Mass-Cruise Drag Trade-off (Wing Loading Optimization)

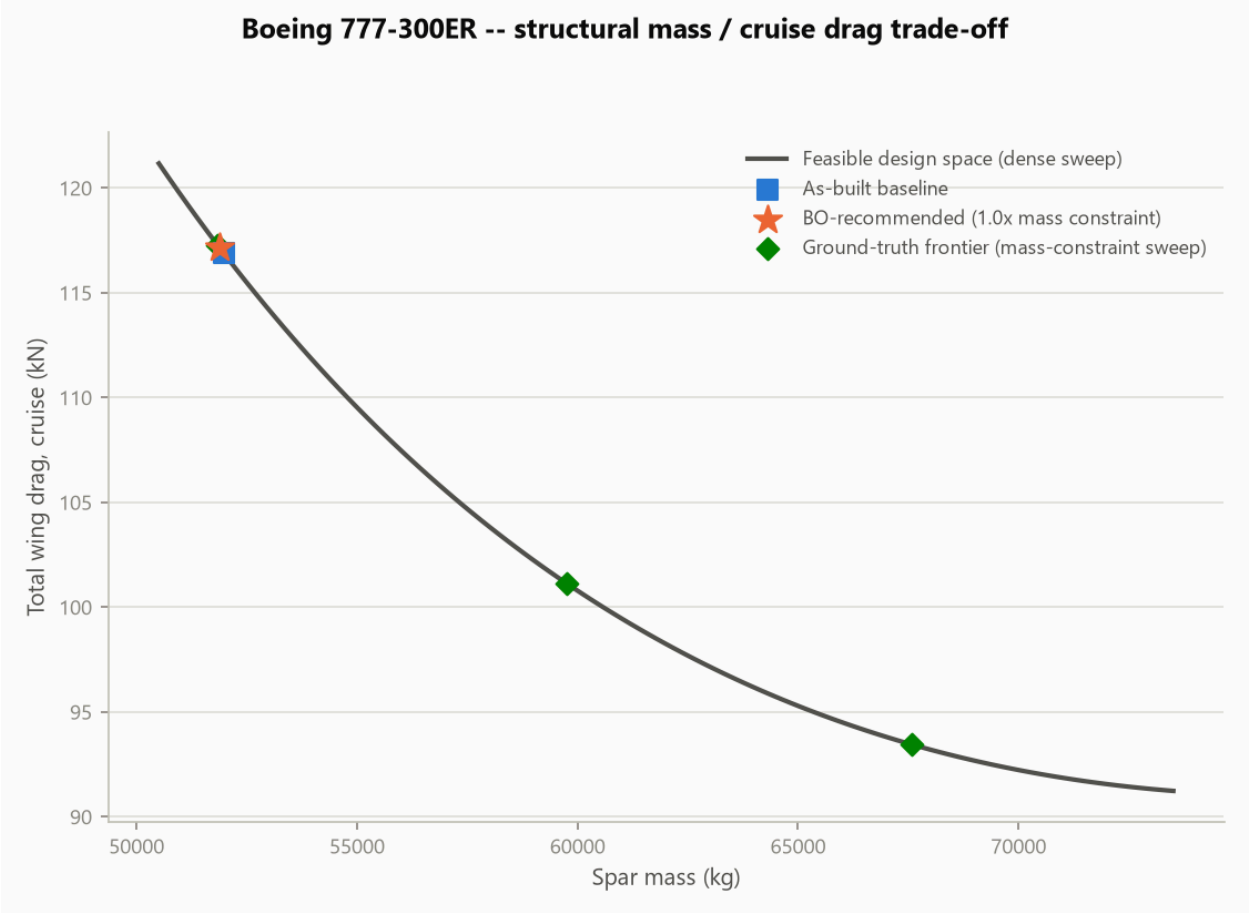


Note. Constrained Bayesian optimization done over wing area for the Airbus A320-200, plotting total wing drag (cruising speed) (kN) against spar mass (kg). The gray curve is the dense feasibility-swept

design space. The orange star is the optimizer's recommendation for improvement for the 1.0x mass constraint.

Figure 7

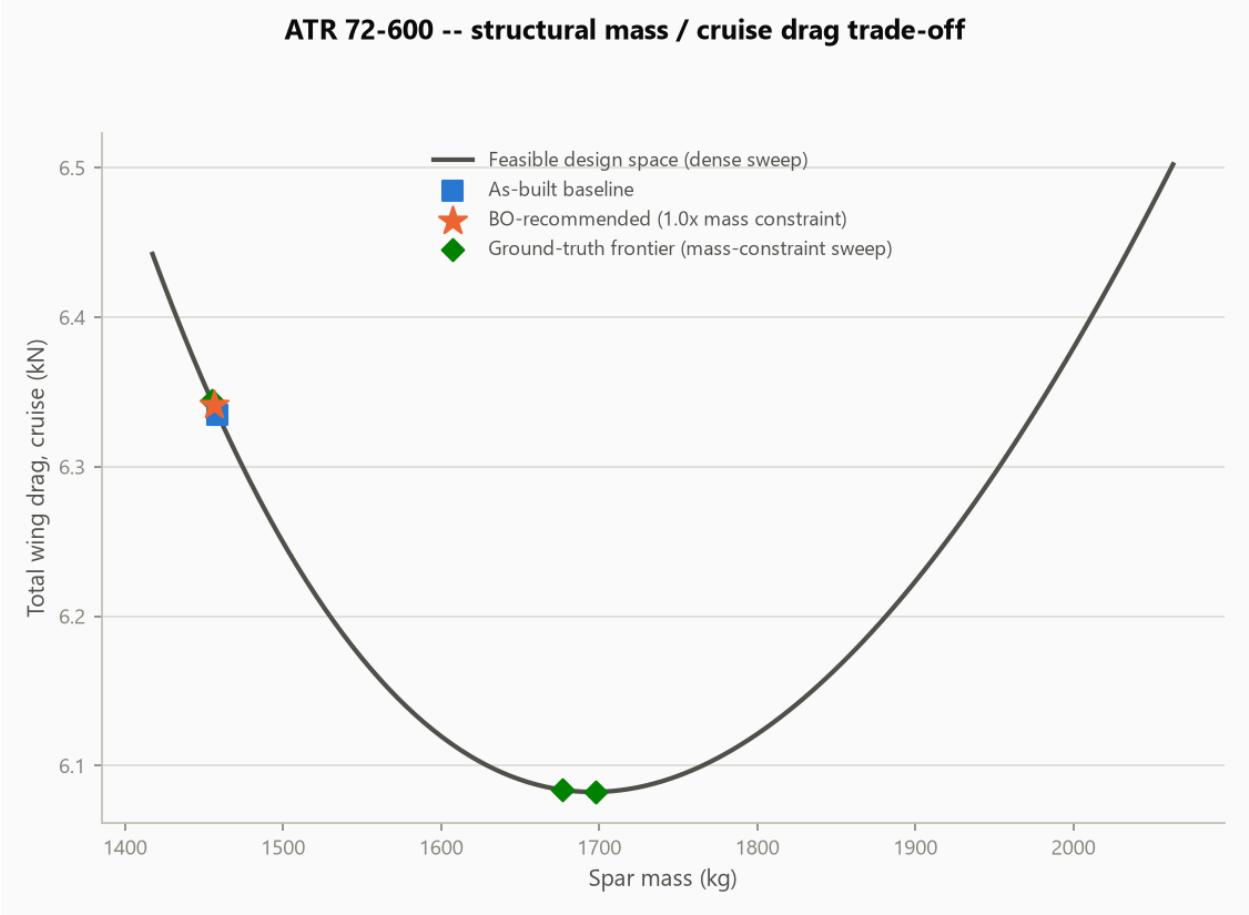
Boeing 777-300ER Structural Mass-Cruise Drag Trade-off (Wing Loading Optimization)



Note. Constrained Bayesian optimization done over wing area for the Boeing 777-300ER, plotting total wing drag (cruising speed) (kN) against spar mass (kg). The gray curve is the dense feasibility-swept design space. The orange star is the optimizer's recommendation for improvement for the 1.0x mass constraint.

Figure 8

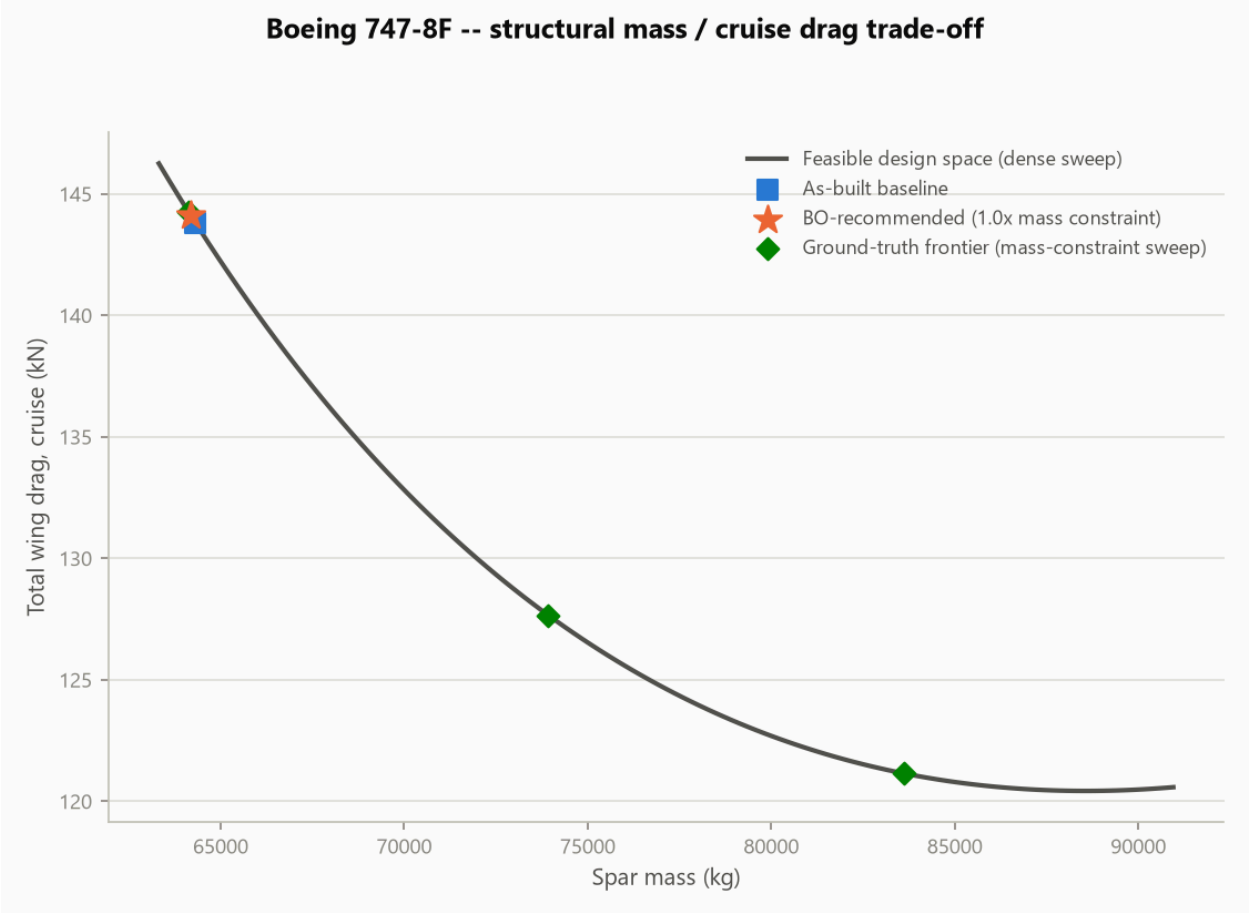
ATR 72-600 Structural Mass-Cruise Drag Trade-off (Wing Loading Optimization)



Note. Constrained Bayesian optimization done over wing area for the ATR 72-600, plotting total wing drag (cruising speed) (kN) against spar mass (kg). The gray curve is the dense feasibility-swept design space. The orange star is the optimizer's recommendation for improvement for the 1.0x mass constraint.

Figure 9

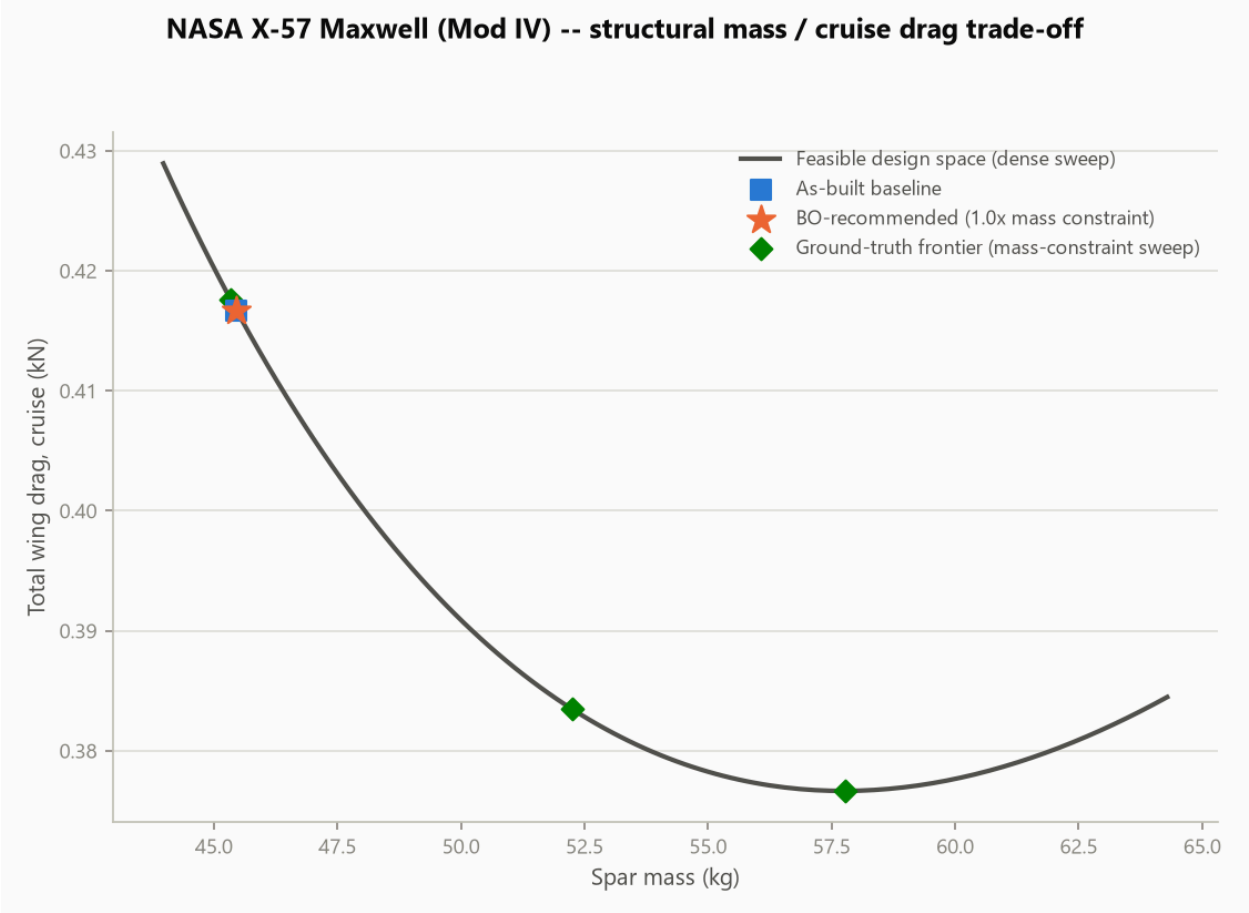
Boeing 747-8F Structural Mass-Cruise Drag Trade-off (Wing Loading Optimization)



Note. Constrained Bayesian optimization done over wing area for the Boeing 747-8F, plotting total wing drag (cruising speed) (kN) against spar mass (kg). The gray curve is the dense feasibility-swept design space. The orange star is the optimizer's recommendation for improvement for the 1.0x mass constraint.

Figure 10

NASA X-57 Maxwell Structural Mass – Cruise Drag Trade-off (Wing Loading Optimization)



Note. Constrained Bayesian optimization done over wing area for the NASA X-57 Maxwell, plotting total wing drag (cruising speed) (kN) against spar mass (kg). The gray curve is the dense feasibility-swept design space. The orange star is the optimizer's recommendation for improvement for the 1.0x mass constraint.

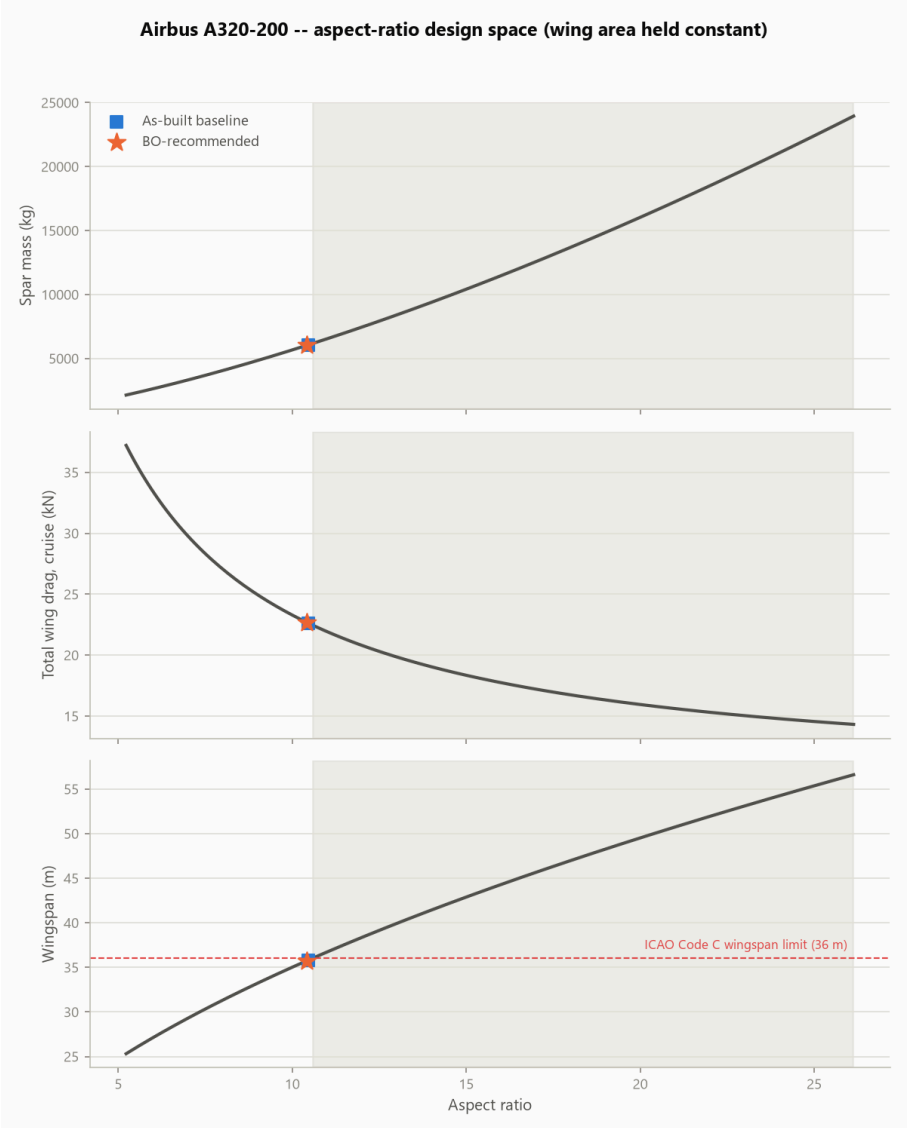
Aspect Ratio Optimization

The aspect ratio model uses the same Gaussian Process as the wing loading module, and also the same constrained Bayesian optimization tools. Contrary to the wing loading model, the aspect ratio model keeps the wing area constant, whilst treating the aspect ratio of the wing as the continuous variable. The span of the wing is calculated as $\sqrt{(AR \times area_0)}$. This model appears more reliable than the wing-loading one, and this is because the spar mass relationship that it needs to fit is not an empirical trend. When beam-theory is applied at a constant wing area, the spar mass is proportional to the aspect ratio raised to the 1.5 power. This relationship has a residual spread of about 2×10^{-15} across all eight aircraft, showcasing how it's derived from the beam-bending equations instead of the unorganized cross-aircraft data. When the same cross-validation as the other surrogate models was applied to the aspect ratio model, it revealed R^2 values of ≈ 1 for mass and drag, with mean absolute error values ranging from 0.0-3.8 kg

for spar mass and 0-5 N for cruise drag. Although the mean absolute error range is larger for this model compared to the wing loading model, this is due to the fact that the relationship between spar mass and aspect ratio of the wing is more nonlinear. Since spar mass rises steeply whilst cruise drag decreases at a steady rate with aspect ratio in this model, the optimal solution is always at the boundary. The optimizer attempts to increase the aspect ratio as much as the mass budget of the wing permits, and although this result seems insignificant, the report compares it to real-life constraints like the ICAO Annex 14 Aerodrome Reference Code (International Civil Aviation Organization [ICAO], 2018). This is a reference code that classifies airports based on the wingspan that they can accommodate. Increasing the aspect ratio raises the wing span while keeping the wing area constant, which means that many aircraft will reach their Aerodrome Reference Code limit before the 1.3x mass one. This constraint divides the aircraft into two categories: those that are span-limited, and those that are mass-limited. The conclusion from this comparison is that aspect-ratio changes are essentially “free” until a certain limit. At this point, the main constraint for many of these airframes is airport infrastructure, rather than the strength or mass limits of the airframes themselves. This conclusion is far different from the other machine learning models that have been a part of this study.

Figure 11

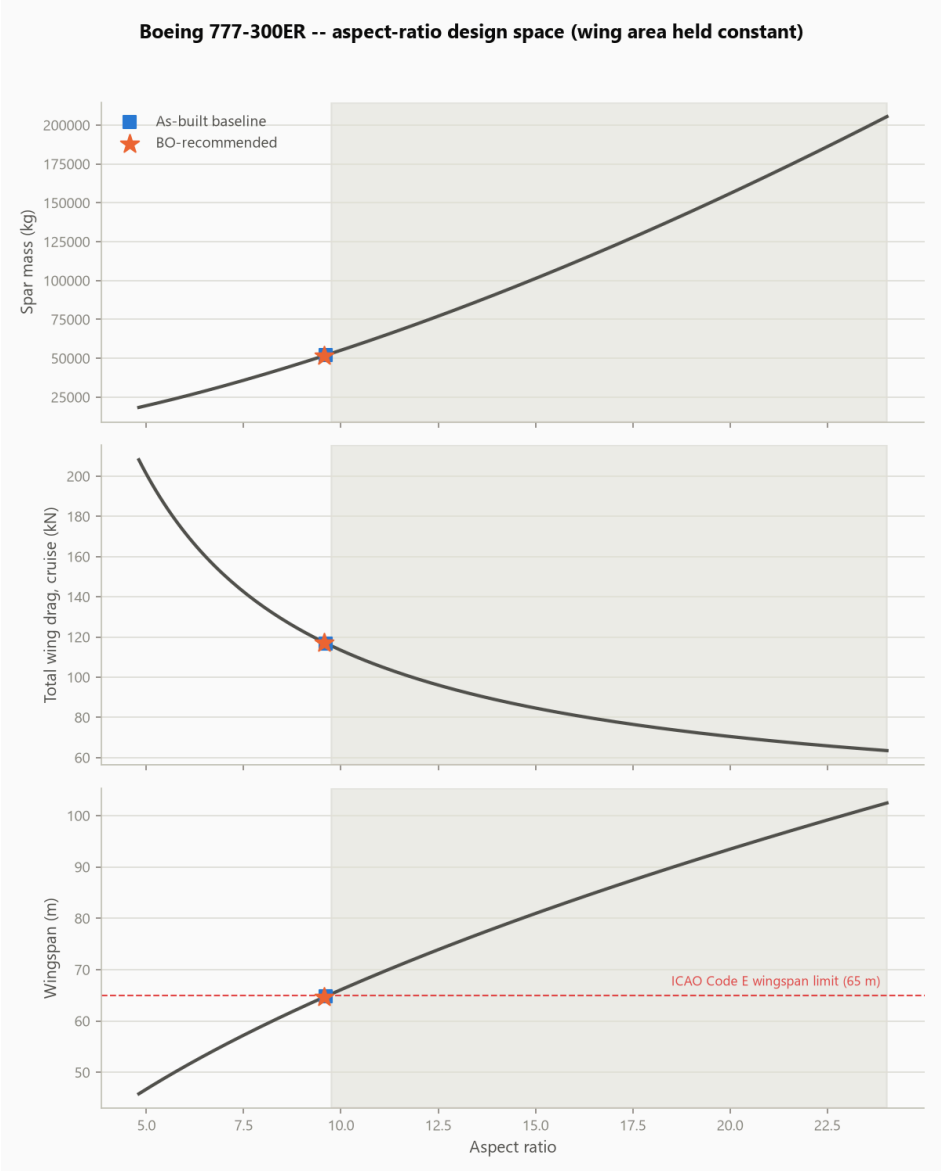
Airbus A320-200 Aspect Ratio Design Space (Wing Area Held Constant)



Note. Constrained Bayesian optimization over aspect ratio for the Airbus A320-200 with constant wing area. Shown graphs are spar mass (kg), cruise wing drag (kN), and wingspan (m) as functions of aspect ratio. The shaded regions show aspect ratios that are past the ICAO Annex 14 Aerodrome Reference Code wingspan limit for the A320-200's category.

Figure 12

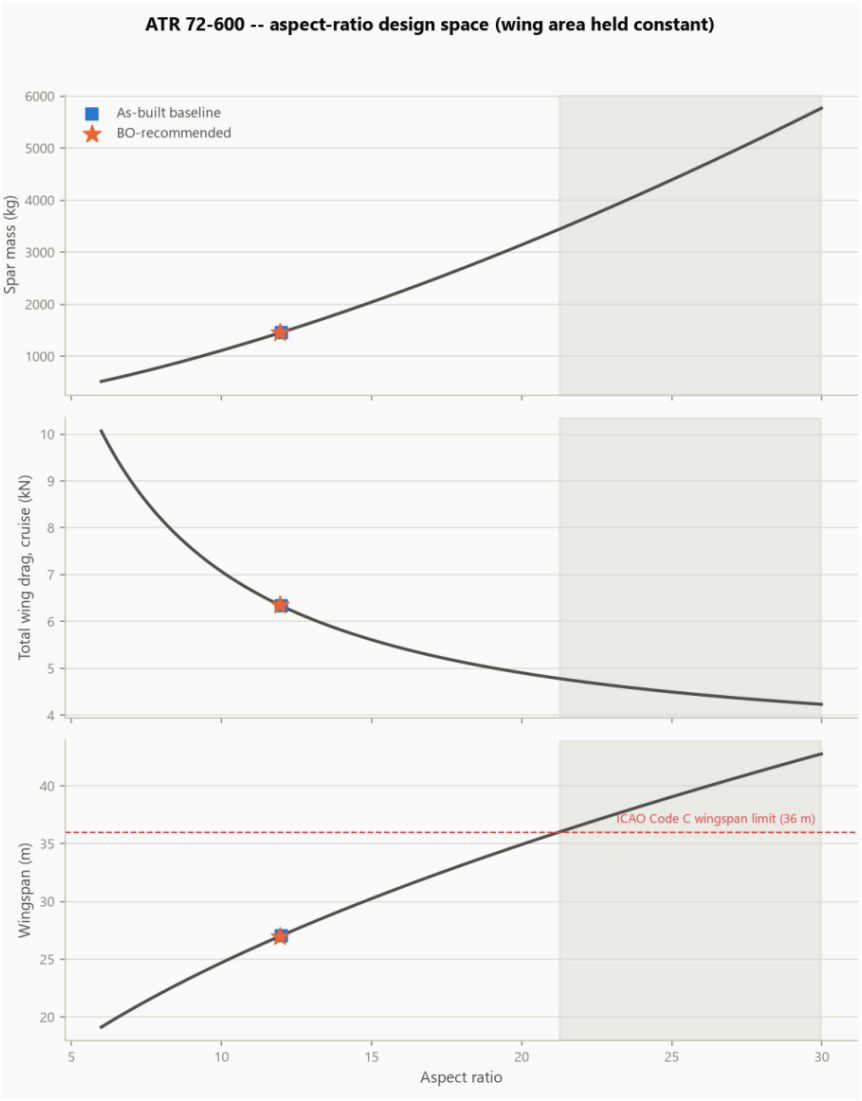
Boeing 777-300ER Aspect Ratio Design Space (Wing Area Held Constant)



Note. Constrained Bayesian optimization over aspect ratio for the Boeing 777-300ER with constant wing area. Shown graphs are spar mass (kg), cruise wing drag (kN), and wingspan (m) as functions of aspect ratio. The shaded regions show aspect ratios that are past the ICAO Annex 14 Aerodrome Reference Code wingspan limit for the 777-300ER's category.

Figure 13

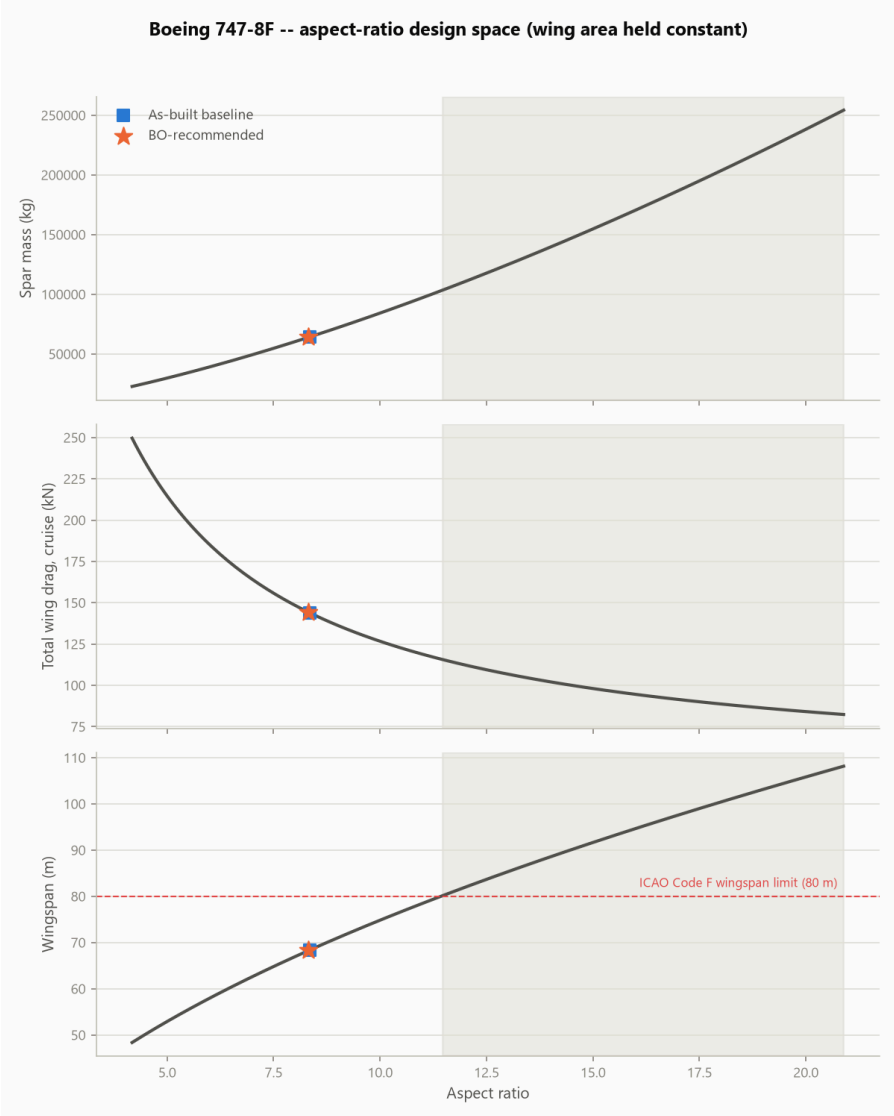
ATR 72-600 Aspect Ratio Design Space (Wing Area Held Constant)



Note. Constrained Bayesian optimization over aspect ratio for the ATR 72-600 with constant wing area. Shown graphs are spar mass (kg), cruise wing drag (kN), and wingspan (m) as functions of aspect ratio. The shaded regions show aspect ratios that are past the ICAO Annex 14 Aerodrome Reference Code wingspan limit for the ATR 72-600's category.

Figure 14

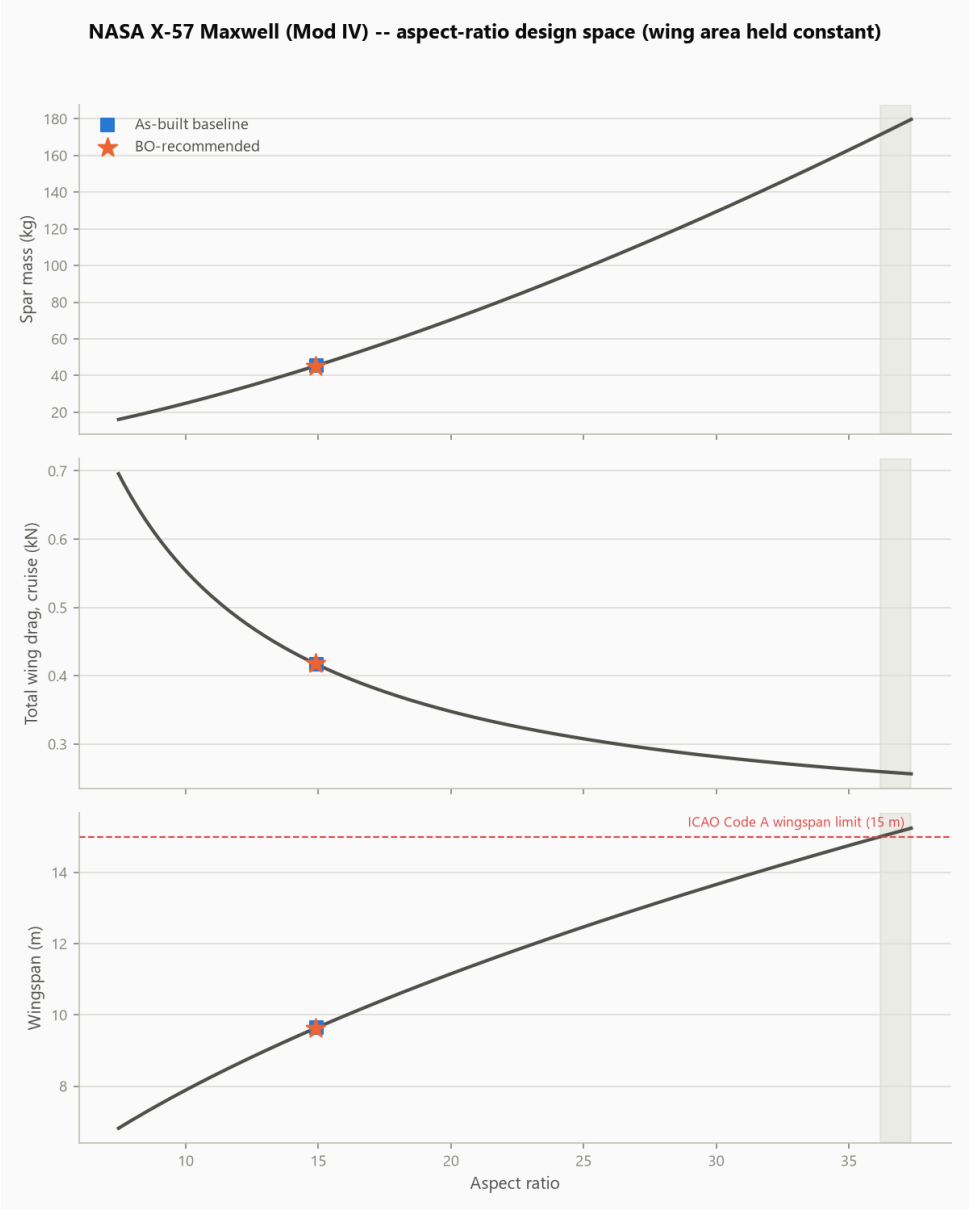
Boeing 747-8F Aspect Ratio Design Space (Wing Area Held Constant)



Note. Constrained Bayesian optimization over aspect ratio for the Boeing 747-8F with constant wing area. Shown graphs are spar mass (kg), cruise wing drag (kN), and wingspan (m) as functions of aspect ratio. The shaded regions show aspect ratios that are past the ICAO Annex 14 Aerodrome Reference Code wingspan limit for the 747-8F's category.

Figure 15

NASA X-57 Maxwell Aspect Ratio Design Space (Wing Area Held Constant)



Note. Constrained Bayesian optimization over aspect ratio for the NASA X-57 Maxwell with constant wing area. Shown graphs are spar mass (kg), cruise wing drag (kN), and wingspan (m) as functions of aspect ratio. The shaded regions show aspect ratios that are past the ICAO Annex 14 Aerodrome Reference Code wingspan limit for the X-57 Maxwell's category.

Limitations of the Regression and Optimization Models

The regression and optimization models used do come with limitations that are worth noting. The size of the aircraft dataset that is analyzed is relatively small when compared to typical machine learning

applications. Despite the use of leave-one-out and five-fold cross-validation to prevent overfitting, the resulting trends should be viewed as directional rather than precise, as the R^2 values were 0.75 and 0.66 for the wing loading and aspect ratio models, respectively. The Classical Lamination Theory and beam-theory idealizations that were used to score the designs do not account for buckling, fatigue, or joint-level effects, and the Gaussian Process surrogates that were used for the wing loading and aspect ratio models are only as accurate as the beam-theory and drag estimates that they were trained on. These limitations were what inspired the following independent CAD/FEA structural check. The Gaussian Process surrogates fit smooth analytical functions, so their R^2 values only show interpolation accuracy. The dataset is a snapshot of ten aircraft whose published specifications mix wing and airframe quantities for composite materials, and the outputs are conceptual-design indications that do not consider additional variables such as manufacturing, cost, certification, etc. The wing-loading drag model holds maximum takeoff weight constant.

The independent CAD/FEA structural check does also have limitations worth stating as well. The idealized two-cap spar model doesn't account for the wing skins, ribs, or torsional stiffness, and does not evaluate the effect of buckling on the compression cap. The load applied was an approximation of the spanwise lift distribution, however this was replaced by two concentrated cap forces (F = M/h) that were applied on the cap face inboard of the load-station plane, with a single fully fixed support representing the wing-to-fuselage attachment. The concentrated load created stress singularities at the sharp-cornered roots, so the peak von Mises values are mesh-dependent and non-physical. The default lowest mesh size (1% of element size) couldn't resolve root fillets, and the mesh-size study (Table 6), covering one load case, did not reach mesh convergence. Verifying the results would therefore rely on section-average cap stress and tip deflection away from these locations, which were not obtained in this study, so the FEA does not validate the sizing. The ATR 72-600, 747-8F, and X-57 models used the transverse force P, and their stresses were scaled to the cap force F. Composite plies were represented with an isotropic-equivalent stiffness (E_x) instead of a full orthotropic laminate model, so the von Mises stress values are a sizing proxy rather than a certified criterion to determine the composite ply's viability. A laminate-level criterion like Tsai-Wu (Tsai & Wu, 1971), or Hashin (Hashin, 1980) first-ply failure would be needed for a certified assessment. Lastly, this study does not evaluate aeroelastic or flutter behavior, which becomes more important for some of the higher aspect ratios that the optimization recommended. Additionally, the compressive strength of CFRP was not checked separately, and the ML layups, with their high 90° ply fraction, have not been evaluated against a laminate failure criterion.

FEA Structural Analysis

All of the regression and optimization models that were created were run across the 10 different aircraft in the dataset, and the CAD/FEA structural check was completed on 5 of those 10 aircraft. Those aircraft are the Airbus A320-200 (narrowbody), Boeing 777-300ER (widebody), ATR 72-600 (regional), Boeing 747-8F (cargo), and the NASA X-57 Maxwell (electric). This selection features one representative aircraft per aircraft category in order to see the results across all of the different types of aircraft. Three models of each aircraft were created and used for testing, all of different materials: Aluminum 7075-T6, a CFRP Baseline, and the ML-optimized CFRP layup. Each of these models were modeled, meshed, and solved under both a cruise (1g) case and a FAR/CS-25.337 Ultimate (3.75g) case. All 15 models were then

rebuilt, applying the corrections described in Methods (combining solids, opposing cap loads, split-face load station), and the results below have replaced the first-pass results. Testing all three materials for each aircraft provides root-stress and spar-mass values for each material composition within every aircraft category. Peak von Mises stress and probe stresses at the root and the load-station seam were recorded for every model. Section-average cap stress and FEA tip deflection could not be obtained reliably, therefore these results do not validate the sizing, and the ultimate-to-cruise peak ratio is solely a solver check. Figures 16-17 are shown here and Figures 18-45 are in the Appendix.

Table 4

Beam-Theory Targets and Rebuilt FEA Results for All 15 Aircraft-Material Cases

Aircraft	Material	Cap area (m^2)	Beam σ cruise/ult. (MPa)	Beam tip defl. (mm)	Peak σ cruise/ult. (MPa)	Peak ratio
A320-200	Al 7075-T6	0.03011	134.1/503.0	554	2,103.9 / 7,872.4	3.74x
A320-200	CFRP	0.02330	173.3/650.0	790	2,904.0 / 9,526.5	3.28x
A320-200	ML CFRP	0.04610	87.6/328.6	554	1,526.4 / 5,724.1	3.75x
777-300ER	Al 7075-T6	0.14273	134.1/503.0	1087	19,253.4 / 72,200.2	3.75x
777-300ER	CFRP	0.11045	173.3/650.0	1549	29,812.8 / 111,797.9	3.75x
777-300ER	ML CFRP	0.21846	87.6/328.6	1087	12,645.2 / 47,419.4	3.75x
ATR 72-600	Al 7075-T6	0.00960	134.1/503.0	400	6,689.0 / 25,087.4	3.75x
ATR 72-600	CFRP	0.00743	173.3/650.0	571	10,031.7 / 37,619.6	3.75x
ATR 72-600	ML CFRP	0.01468	87.7/328.8	400	2,817.3 / 10,566.4	3.75x
747-8F	Al 7075-T6	0.16731	134.1/503.0	1003	27,604.1 / 103,512.8	3.75x
747-8F	CFRP	0.12947	173.3/650.0	1430	43,480.7 / 163,048.1	3.75x
747-8F	ML CFRP	0.25677	87.4/327.7	1003	17,330.5 / 64,991.0	3.75x
X-57	Al 7075-T6	0.00084	134.1/503.0	194	6,453.1 / 24,197.4	3.75x

X-57	CFRP	0.00065	173.3/650.0	276	9,759.0 / 36,596.8	3.75x
X-57	ML CFRP	0.00131	85.9/322.1	194	2,588.0 / 9,703.3	3.75x

Note. Beam σ ultimate is the max sizing allowable, and the cruise is that divided by 3.75. Beam tip deflection values are the cruise prediction values from the case files. FEA peak values are mesh-dependent maxima at singular locations (see Methods) and are not a measure of agreement. The 777-300ER peaks are from solving using cap force F. The ATR 72-600, 747-8F, and X-57 peaks were solved using the transverse force P and multiplied by F/P (11.52, 10.22 and 16.89).

Table 5 lists the probed stress values from the rebuilt-models (Figures 16-45) at the root and load-station probes, placed on both the upper and lower caps, for both the cruise and ultimate cases. These probes are in the singular regions described in Methods, so they are not section-average stresses and do not validate the sizing. Probes also snap to the nearest mesh node, so their positions differ between models and between load cases, and their cruise-to-ultimate ratios are not always 3.75x. They instead show how local the stress field is, as on the A320, the load-station probes read about 266-974 MPa, when their beam-theory targets were 88-650 MPa. On the 777-300ER the model's force acts over the inboard cap face up to the load-station plane, so the axial force falls to nearly 0 at the station-seam probes. The ATR 72-600, 747-8F, and X-57 values in Table 5 are the P-solution probe values multiplied by F/P.

Table 5

Probe Stresses (MPa) from the Rebuilt Fusion 360 Models, Cruise / Ultimate

Aircraft	**Material**	**Root, Upper Cap**	**Root, Lower Cap**	**Seam, Upper Cap**	**Seam, Lower Cap**
A320-200	Al 7075-T6	245.3 / 134.2	223.6 / 969.9	266.5 / 374.5	348.2 / 737.4
A320-200	CFRP	624.3 / 950.9	285.2 / 902.3	343.8 / 732.5	436.1 / 974.3
A320-200	ML CFRP	184.7 / 687.1	103.2 / 692.5	265.5 / 439.1	176.4 / 657.7
777-300ER	Al 7075-T6	615.9 / 4,829.8	2,030.4 / 13,109.1	2.07 / 5.78	0.63 / 2.31
777-300ER	CFRP	1,788.2 / 14,824.6	4,844.9 / 33,801.1	0.63 / 7.76	0.76 / 3.15
777-300ER	ML CFRP	1,793.9 / 5,434.6	1,259.5 / 9,083.0	0.64 / 1.06	0.66 / 3.20
ATR 72-600	Al 7075-T6	1,281.3 / 13,133.7	1,745.7 / 5,698.0	22.4 / 119.8	34.3 / 74.8

ATR 72-600	CFRP	4,853.4 / 16,803.7	6,156.6 / 24,027.3	39.3 / 54.4	49.5 / 197.0
ATR 72-600	ML CFRP	63.6 / 312.3	44.2 / 940.3	22.1 / 1,000.2	24.2 / 31.7
747-8F	Al 7075-T6	642.1 / 3,394.4	426.4 / 18,812.1	40.0 / 163.6	61.8 / 202.4
747-8F	CFRP	2,569.4 / 17,716.0	9,942.3 / 15,145.6	62.9 / 176.9	31.7 / 103.3
747-8F	ML CFRP	296.5 / 3,635.8	1,474.4 / 1,692.2	16.4 / 72.8	7.46 / 65.7
X-57	Al 7075-T6	4,238.4 / 9,863.8	1,153.8 / 14,500.9	15.7 / 48.7	4.22 / 60.5
X-57	CFRP	4,588.1 / 7,076.4	618.3 / 30,658.9	8.45 / 41.4	26.7 / 111.8
X-57	ML CFRP	442.6 / 714.6	1,101.4 / 5,206.4	6.76 / 29.1	11.7 / 43.4

Note. Values are von Mises stress values, in MPa, at the probe labels visible in Figures 16-45, listed as cruise / ultimate. Root probe placement: A320 x = 1,644 mm, y = -700 mm; 777-300ER x = 3,513 mm, y = -1290 mm; ATR 72-600 x = 762 mm, y = -500 mm; 747-8F x = 4,215 mm, y = -1420 mm; X-57 x = 200 mm, y = -120 mm. Load-station probe placement: A320 x = 4,101 mm, y = -7230 mm; 777-300ER x = 9,956 mm, y = -13,094 mm; ATR 72-600 x = 604 mm, y = -5,486 mm; 747-8F x = 12,857 mm, y = -13,792 mm; X-57 x = 169 mm, y = -1983 mm. Values for the ATR 72-600, 747-8F, and X-57 were solved using the transverse force P and multiplied by F/P.

To evaluate mesh sensitivity, the A320-200 aluminum cruise case was re-solved with absolute element sizes of 40, 20, and 10 mm (see Table 6). The peak von Mises stress fell from 3,131 to 2,097 to 1,798 MPa, and every probe fell by 35-77% between meshes (20-to-10 mm drop was 71-77%). Due to the 45 mm aluminum cap being about one element thick at 40 mm, the coarse meshes overstate stress, and as the mesh gets finer, the trend goes towards the 134.1 MPa beam-theory target (the 10 mm probes read 61-151 MPa). However, these values still can not be treated as converged because the probes are changing rapidly, the 1,798 MPa peak is 13 times the target, and the upper-spar probe values differ from the lower-spar probe values. Therefore, a finer mesh, or a local size control on the spars, is needed before the section-average stress can be reported.

Table 6

Mesh Sensitivity, A320-200 Aluminum 7075-T6, Cruise (1g): von Mises Stress (MPa)

Element Size	Peak Stress	Root Stress, Upper Cap	Root Stress, Lower Cap	Seam Stress, Upper Cap	Seam, Lower Cap
40 mm	3,130.6	472.2	1,033.2	419.0	717.0
20 mm	2,096.6	251.5	593.1	273.2	324.1
10 mm	1,797.7	61.0	151.2	63.6	92.8
Change, 20 to 10 mm	-14%	-76%	-75%	-77%	-71%

Note. Beam-theory target stress value: 134.1 MPa. Root probe: x = 1,644 mm, y = -700 mm; seam-station probe: x = 4,101 mm, y = -7,230 mm. Probes placed on both upper and lower spars. An 8 mm mesh exceeded maximum element count so mesh sensitivity study capped at 10 mm.

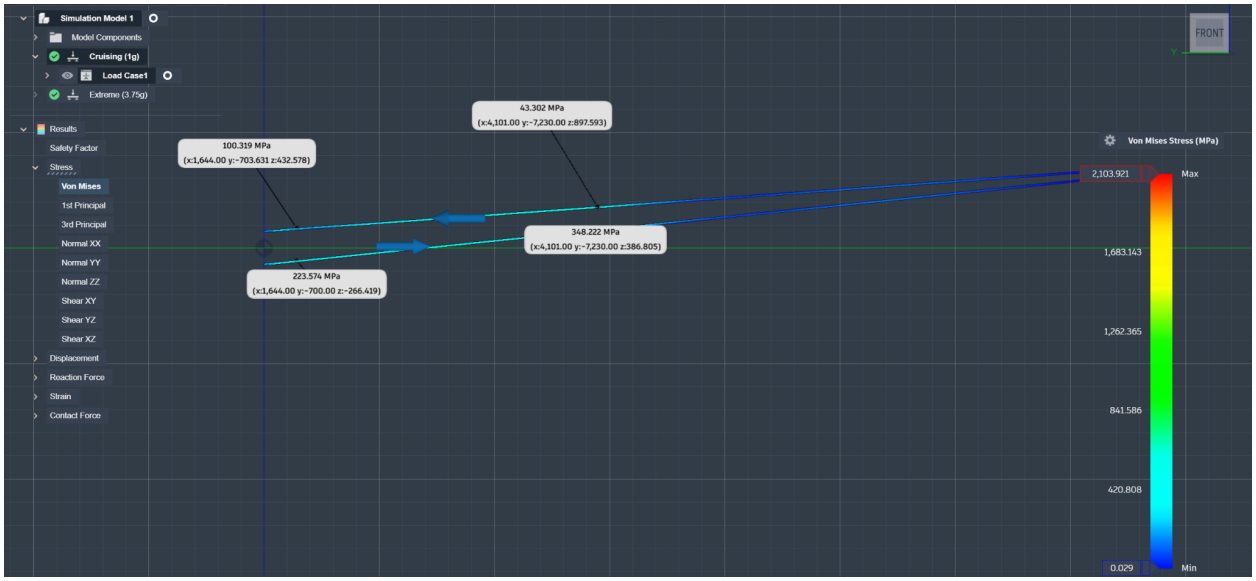
Airbus A320-200

The A320 model showcases how the beam-theory model works, which is by taking the root bending moment and converting it to an axial tension and compression pair. This pair is carried by the two spar caps, which are separated by the wingbox height, ensuring that each spar cap re-creates a real axial force instead of a bending stress stretched across the wing. For the A320, this yielded a root bending moment of 10,876,198 N•m at the ultimate (3.75g) load case, derived from the FAR/CS 25.337 2.5g limit maneuvering load factor multiplied by the FAR/CS 25.303 1.5 safety factor, a root wingbox height of 0.718 m, and cap axial forces of 15,146,700 N and 4,039,120 N for the 3.75g and 1g load cases, in that order.

These forces were then applied to the three different models, starting with the Aluminum 7075-T6 model. For this model, the cruise (1g) load case reported a maximum von Mises stress of 2,103.9 MPa, and the ultimate (3.75g) load case reported a maximum von Mises stress of 7,872.4 MPa (Figures 16-17). When compared to a target of 134.1 MPa for the cruise load case and 503 MPa (the yield strength of the material rather than its higher ultimate tensile strength) for the ultimate load case. The peaks are therefore about 15.7 times the targets, and this also produced an ultimate-to-cruise ratio of 3.74x: close to the 3.75x expected under FAR/CS-25.337. This confirms the load cases but is not a validation of the beam-theory sizing. Probes were placed at both the root and load-station-seam for each of the spars in the model, ensuring that the (x, y) coordinates, accounting for the sweep angle of the wing, lined up properly. At the root, x = 1,644 mm and y = -700 mm, and at the load-station seam the probes were placed at x = 4,101 mm and y = -7,230 mm. The probed values (Table 5) are local readings in the singular regions and are not section-average stresses. The load-station probes read 266.5-348.2 MPa at cruise and 374.5-737.4 MPa at ultimate, and when compared to the expected 134.1 and 503.0 MPa, this is consistent with their proximity to the point-load application.

Figure 16

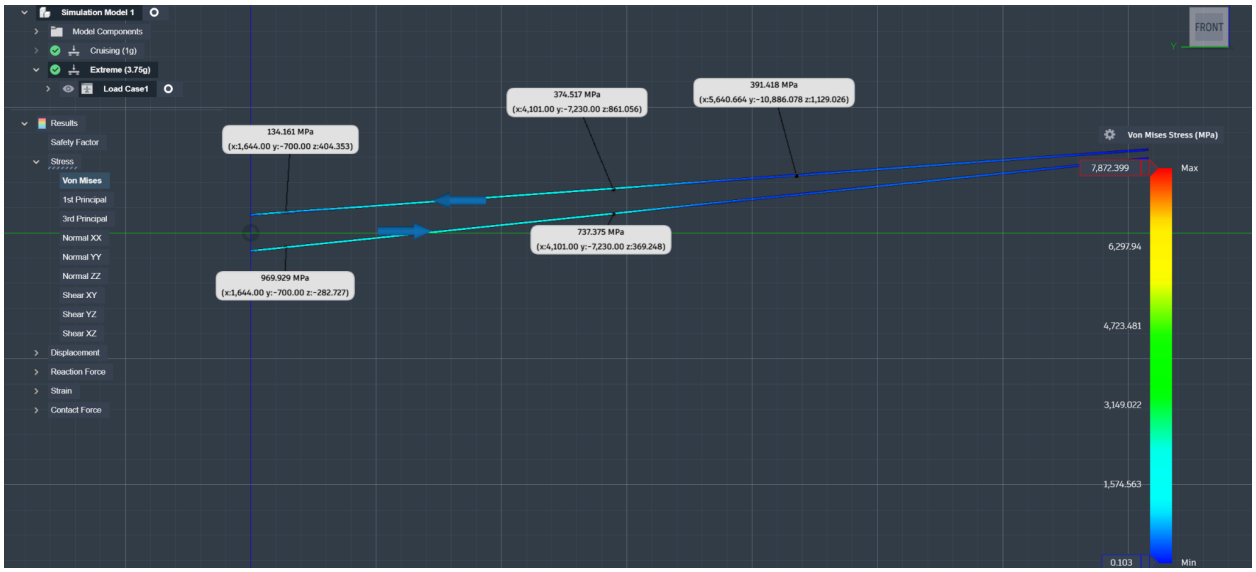
A320-200 Wing Spar (Aluminum 7075-T6) – von Mises Stress, Cruise (1g) Load Case



Note. Autodesk Fusion 360 static stress study, von Mises stress distribution for the A320-200 spar-cap model (Aluminum 7075-T6) under the cruise (1g) case. Global maximum stress: 2,103.9 MPa.

Figure 17

A320-200 Wing Spar (Aluminum 7075-T6) – von Mises Stress, Ultimate (3.75g) Load Case



Note. Autodesk Fusion 360 static stress study, von Mises stress distribution for the A320-200 spar-cap model (Aluminum 7075-T6) under the Ultimate (3.75g) load case. Global maximum stress: 7,872.4 MPa.

The remaining A320 material configurations – the representative-CFRP Baseline layup and the ML-optimized layup – follow the same two spar-cap idealization and the same load cases as the Aluminum model above. This time, however, the models make use of the CFRP material properties that

were established previously: E_x, allowable stress, and density. Both materials' results are described below, along with a mass and stress comparison against Aluminum.

For the CFRP Baseline, the rebuilt model reported a global maximum von Mises stress value of 2,904.0 MPa and 9,526.5 MPa for the cruise and ultimate load cases, respectively (Figures 18-19). The targets for these cases were 173.3 MPa and 650.0 MPa, respectively, and as a result these values were about 16.8 and 14.7 times the target values). The ultimate-to-cruise ratio was 3.28x instead of the expected 3.75x from a linear solver. This is an anomaly, and so the CFRP Baseline results should be treated with caution. The root probes (Table 5) read 624.3 MPa for the upper cap cruise case and 950.9 MPa for the upper cap ultimate case, and read 285.2 MPa and 902.3 MPa for the lower cap cruise and ultimate cases, respectively. The seam probes (Table 5) read 343.8 MPa and 732.5 MPa for the upper cap for the cruise and ultimate cases, respectively, and 436.1 MPa and 974.3 MPa for the lower cap cases, in that order. However, these are local readings and do not validate the beam-theory sizing.

For the ML-Optimized layup, the global maximum von Mises stress was 1,526.4 MPa for the cruise load case and 5,724.1 MPa for the ultimate load case (Figures 20-21). The targets were 87.6 MPa and 328.6 MPa (both cases were about 17.4 times the targets), but they had the 3.75x ultimate-to-cruise ratio. The root probes (Table 5) had values of 184.7 MPa and 687.1 MPa for the cruise and ultimate cases, respectively, of the upper root probe, and 103.2 MPa and 692.5 MPa for the cruise and ultimate cases, respectively, of the lower root probe. The seam probes (Table 5) had values of 265.5 MPa and 439.1 MPa for the upper cap for the cruise and ultimate cases, as well as 176.4 MPa and 657.7 MPa for the cruise and ultimate cases, respectively, of the lower cap.

Results for the Remaining Aircraft

The remaining four aircraft were also sized making use of the same beam-theory sizing routine ($F = M/h$, $A = F/\sigma_{allow}$) and were also tested on all three materials from the previous A320-200 testing. All of the remaining aircraft also used the same two-cap spar design used for the A320 models which provided an actual face in the model in the middle of the wing for the force to be attached to. For all three materials, the geometry and loading are the same for a given aircraft, with only the required spar-cap area changing. To compensate for this, the cap thickness for each material is changed for each model. The stress targets for all of the Aluminum and baseline CFRP tests are the same because the materials' allowable stress levels are independent of the aircraft type and size, but the ML-Optimized CFRP targets vary for each aircraft because the CFRP layups were optimized individually for each aircraft. Like with the A320-200, the global maximum von Mises stress, as well as additional stress probing at the root and load-station seam of the wing, has been reported for each remaining aircraft. For the 777-300ER model, the cap force acts over the inboard cap face up to the load-station plane, and it was solved at the cap force F. The other aircraft were solved at the transverse force P, and had their stress values multiplied by F/P, so that their stresses are at the cap force F, although the contour figures in the Appendix show the unscaled P solutions.

The Boeing 777-300ER model featured a wingspan of 64.8 m, a root chord length of 11.235 m, a root wingbox height of 1.236 m, and the load was placed 13.738 m away from the root of the wing. The cap

force was 19,145,052 N for the cruise load case, and 71,793,945 N for the ultimate load case. The required spar-cap area at the root is 0.14273 m^2 for Aluminum 7075-T6, 0.11045 m^2 for the CFRP Baseline, and 0.21846 m^2 for the ML-Optimized CFRP layup.
The reported maximum global von Mises stress for Aluminum had values of 19,253.4 MPa and 72,200.2 MPa for the cruise and ultimate load cases compared to target values of 134.1 MPa and 503.0 MPa. For the CFRP Baseline, the reported maximums were 29,812.8 MPa and 111,797.9 MPa versus targets of 173.3 MPa and 650.0 MPa. For the ML-Optimized CFRP layup, the reported maximums were 12,645.2 MPa and 47,419.4 MPa versus targets of 87.6 MPa and 328.6 MPa. These values are ~144, ~172, and ~144 times the targets for the Aluminum, CFRP Baseline, and ML-Optimized CFRP, respectively, which is far greater than the ratios of about 15 to 17 seen for the A320-200. Therefore, the 777-300ER peaks can not be interpreted as cap stresses, and the difference between the two aircraft was not resolved.

Probes were placed at both the root and seam on the spars for all three materials at the same coordinates: x = 3,513 mm and y = -1,290 mm for the root and x = 9,956 mm and y = -13,094 mm for the seam. For the three materials, the stress at the root for the cruise load case ranged between 615.9 and 4,844.9 MPa and from 4,829.8 to 33,801.1 MPa for the ultimate load case. At the seam, the probed stress ranged from 0.63 to 2.07 MPa for the cruise load case and from 1.06 to 7.76 MPa for the ultimate load case. This is expected because the force acts over the inboard cap face up to the load-station plane, which means that the axial force is nearly 0 at the station which the seam probes sit just inboard from. The 3.75x ratio doesn't hold for the probed stress values, as they land on different mesh nodes in each model, so the probes are local readings and do not validate the beam-theory sizing.

The ATR 72-600 model featured a wingspan of 27.05 m, a root chord length of 3.111 m, a root wingbox height of 0.498 m, and the load was placed 5.735 m away from the root of the wing. The cap force was 1,287,140 N for the cruise load case, and 4,826,775 N for the ultimate load case (although the model was solved with equivalent transverse forces of 111,704 N and 418,888 N and the stresses multiplied by F/P = 11.52). The required spar-cap area at the root is 0.00960 m^2 for Aluminum 7075-T6, 0.00743 m^2 for the CFRP Baseline, and 0.01468 m^2 for the ML-Optimized CFRP layup.

The reported maximum von Mises stress for Aluminum was 6,689.0 MPa for the cruise load case and 25,087.4 MPa for the ultimate load case versus targets of 134.1 MPa and 503.0 MPa. The reported maximum for the CFRP Baseline is 10,031.7 MPa and 37,619.6 MPa for the cruise and ultimate load cases, respectively, versus targets of 173.3 MPa and 650.0 MPa. The reported maximums for the ML-Optimized CFRP were 2,817.3 MPa and 10,566.4 MPa for the cruise and ultimate load cases, respectively, versus targets of 87.7 MPa and 328.8 MPa. These are ~50, ~58, and ~32 times the targets for Aluminum, CFRP Baseline, and ML-Optimized CFRP, respectively. This means that they are singular peaks and cannot be interpreted as cap stresses.

Probes were placed at both the root and seam on the spars for all three materials at the same coordinates: x = 762 mm and y = -500 mm for the root and x = 604 mm and y = -5,486 mm for the seam. After scaling to the cap force F, the stress at the root for the cruise load case ranged between 44.2 and 6,156.6 MPa and from 312.3 to 24,027.3 MPa for the ultimate load case. At the seam, the probed stress ranged from 22.1 to

49.5 MPa for the cruise load case and from 31.7 to 1,000.2 MPa for the ultimate load case. These are local readings at nodes that differ between models, so they are not section-average stresses, their ratios between load cases do not equal 3.75x, and do not validate the beam-theory sizing.

The Boeing 747-8F model featured a wingspan of 68.40 m, a root chord length of 12.893 m, a root wingbox height of 1.418 m, and the load was placed 14.501 m away from the root of the wing. The cap force was 22,441,477 N for the cruise load case, and 84,155,539 N for the ultimate load case (the model was solved at the equivalent transverse forces of 2,194,876 N and 8,230,785 N, and the stresses were multiplied by F/P = 10.22). The required spar-cap area at the root is 0.16731 m^2 for Aluminum 7075-T6, 0.12947 m^2 for the CFRP Baseline, and 0.25677 m^2 for the ML-Optimized CFRP layup.

The reported maximum von Mises stress for Aluminum was 27,604.1 MPa for the cruise load case and 103,512.8 MPa for the ultimate load case versus targets of 134.1 MPa and 503.0 MPa. The reported maximum for the CFRP Baseline is 43,480.7 MPa and 163,048.1 MPa for the cruise and ultimate load cases, respectively, versus targets of 173.3 MPa and 650.0 MPa. The reported maximums for the ML-Optimized CFRP were 17,330.5 MPa and 64,991.0 MPa for the cruise and ultimate load cases, respectively, versus targets of 87.4 MPa and 327.7 MPa. These are ~206, ~251, and ~198 times the targets for Aluminum, CFRP Baseline, and ML-Optimized CFRP, respectively. This means they are singular peaks that cannot be interpreted as cap stresses.

Probes were placed at both the root and seam on the spars for all three materials at the same coordinates: x = 4,215 mm and y = -1,420 mm for the root and x = 12,857 mm and y = -13,792 mm for the seam. After scaling to the cap force F, the stress at the root for the cruise load case ranged between 296.5 and 9,942.3 MPa and from 1,692.2 to 18,812.1 MPa for the ultimate load case. At the seam, the probed stress ranged from 7.46 to 62.9 MPa for the cruise load case and from 65.7 to 202.4 MPa for the ultimate load case. These are local readings at nodes that differ between models, so they are not section-average stresses, their ratios between load cases do not equal 3.75x, and do not validate the beam-theory sizing.

The NASA X-57 Maxwell model featured a wingspan of 9.64 m, a root chord length of 0.807 m, a root wingbox height of 0.121 m, and the load was placed 2.044 m away from the root of the wing. The cap force was 112,556 N for the cruise load case, and 422,086 N for the ultimate load case (the model was solved at the equivalent transverse forces of 6,663 N and 24,986 N, and the stresses were multiplied by F/P = 16.89). The required spar-cap area at the root is 0.00084 m^2 for Aluminum 7075-T6, 0.00065 m^2 for the CFRP Baseline, and 0.00131 m^2 for the ML-Optimized CFRP layup.

The reported maximum von Mises stress for Aluminum was 6,453.1 MPa for the cruise load case and 24,197.4 MPa for the ultimate load case versus targets of 134.1 MPa and 503.0 MPa. The reported maximum for the CFRP Baseline is 9,759.0 MPa and 36,596.8 MPa for the cruise and ultimate load cases, respectively, versus targets of 173.3 MPa and 650.0 MPa. The reported maximums for the ML-Optimized CFRP were 2,588.0 MPa and 9,703.3 MPa for the cruise and ultimate load cases, respectively, versus targets of 85.9 MPa and 322.1 MPa. These are ~48, ~56, and ~30 times the targets for Aluminum, CFRP

Baseline, ML-Optimized CFRP, respectively. This means that they are singular peaks that cannot be interpreted as cap stresses.

Probes were placed at both the root and seam on the spars for all three materials at the same coordinates: x = 200 mm and y = -120 mm for the root and x = 169 mm and y = -1,983 mm for the seam. After scaling to the cap force F, the stress at the root for the cruise load case ranged between 442.6 and 4,588.1 MPa and from 714.6 to 30,658.9 MPa for the ultimate load case. At the seam, the probed stress ranged from 4.22 to 26.7 MPa for the cruise load case and from 29.1 to 111.8 MPa for the ultimate load case. These are local readings at nodes that differ between models, so they are not section-average stresses, their ratios between load cases do not equal 3.75x, and do not validate the beam-theory sizing.

DISCUSSION

Across the ten-aircraft dataset, the clearest finding was that changing the wing material composition would have the most profound effects whilst being reasonably actionable. Seven of the ten aircraft have composite fractions below their aircraft category's modern composite-fraction target, and this means that they may be carrying more structural wing weight than necessary. The wing loading and aspect ratio models' optimization results were more complex though, because the wing loading optimum was nearly mass-neutral when using the most conservative constraints. Furthermore, the aspect ratio optimum was a boundary solution that was limited by airport infrastructure capabilities rather than wing structural mass, which was also unexpected.

The CAD/FEA check is a somewhat weak confirmation. The ultimate-to-cruise peak-stress ratio was 3.75x in 14 out of the 15 rebuilt models (3.74x for A320 aluminum and 3.28x for A320 CFRP Baseline), but a linear solver would return that ratio for any correct load application, regardless of the sizing. This means that all these ratios confirm the load cases and not the beam-theory itself. The peak stresses were about 15 to 250 times above the sizing targets at singular locations, and are not interpreted. The quantities that could validate the sizing are the section-average cap stress and the tip deflection when compared to the beam-theory targets, but these could not be obtained reliably from the present models, so the sizing remains unvalidated by the FEA. Refining the A320 aluminum mesh lowered the peak stress and probed stress values, therefore the solution is not mesh-converged and the peaks reflect singularities. The FEA therefore, is best read as a check that the geometry, constraints, and load cases were applied consistently, not proof of the beam-theory sizing.

The 11-13% spar-cap mass saving for the stiffness-matched CFRP layup is a simplified caps-only sizing result. It should be put alongside published aluminum-to-composite wing mass savings. NASA's composite transport wing programs report ~35% savings for graphite/epoxy upper covers and ~37% for spars relative to aluminum baselines (Griffin & Harvill, 1988). Boeing's later AST program compared a composite wing box against an aluminum design that was identical (Karal, 2001), and Korba et al. (2024) compares aluminum and CFRP wing-box panels. The figure in this study is lower than these values, however, and this is consistent with the methods used rather than a contradiction to them. Firstly, it only covers the untapered, sized-at-the-root spar-caps instead of full wingboxes with skins, stringers, ribs, and

joints. In practice, these are places where composite weight benefits would play the largest role, but in this study this isn't evaluated. Secondly, the layup is constrained to match the aluminum cruise case tip deflection, meaning that the composite has to be as stiff as the aluminum baseline. This stiffness requirement actually ends up counteracting the strength-driven weight savings that the composite material has. Third, the layups use a ply-fraction strength rule instead of a first-ply failure or knock-down criterion, which is why the magnitude is consistent with a lower bound for the spar-only case, and should not be used as a representation of whole-wing mass savings.

Newer designs already show the direction of these recommendations: the A350-900 already meets its category's composite target (Table 2), and the 777X replaces the 777-300ER's aluminum wing with a composite wing and folding wingtips (71.8 m extended and 64.8 m folded) (Boeing Commercial Airplanes, n.d.). The 787, A220, and 777X are not in the dataset and would be natural next steps. It is important to note that these recommendations do not address certification, manufacturing, or cost–important aspects in determining the practicality of any changes.

CONCLUSION

This study aimed to test whether or not a set of regression and optimization models built from real, publicly documented aircraft, instead of simulated data, could produce useful and feasible improvements for aircraft wing design, and also validate those recommendations with CAD structural analysis and FEA. The results suggest that it is possible, as all three proxy models generated results that were not only statistically possible, but also followed known aerospace engineering principles. The CAD/FEA check confirmed that the load cases were applied consistently, as the peak stress scaled with the load, but since the peak stresses were dominated by singularities, they cannot be used to support the beam-theory sizing. The beam-theory sizing therefore remains unvalidated by the FEA, and the section-average stress and tip-deflection comparison is left for future work. These findings matter because a wing with more structural weight than the target for its aircraft category indicates that it is carrying unnecessary weight on every flight. Reducing aircraft mass is one of the most direct ways of reducing fuel burn and CO_2 emissions, so the seven aircraft that are currently below their category's wing composite material fraction target are areas where the negative environmental effects discussed in the Introduction could be improved upon.

Future work with this study would likely start with thermal loading, given the different coefficients of thermal expansion for Aluminum 7075-T6 and CFRP layups at different temperatures. Another possible step could be expanding the dataset beyond ten aircraft, and if more publicly documented wingbox data is available in the future, it would increase the confidence in all optimization models. The FEA should also be repeated with CAD model changes such as a distributed spanwise load and a tapered multi-cell wingbox with full skin and ribs. Additionally, the new FEA runs should feature additional testing changes such as a full mesh-convergence study for every aircraft and load case, with root fillets and laminate failure criteria. The new FEA runs should also include checks for buckling, fatigue, and aeroelasticity. It should first be repeated with the cap force applied at the load station, extracting section-average cap stress

and tip deflection away from the singular regions. The dataset should also be expanded to include more modern designs, such as the 787, A220, and 777X.

REFERENCES

Airbus. (2024). *Aircraft Characteristics- Airport and Maintenance Planning*. https://aircraft.airbus.com/sites/g/files/jlcbta126/files/2024-06/AC_A320_0624.pdf

Airbus. (2025a). A350 Family: The Long Range Leader. In *Airbus.com*. https://www.airbus.com/sites/g/files/jlcbta136/files/2025-04/Airbus-A350-Family-Facts-and-Figures-April-2025.pdf

Airbus. (2025b, August 7). *Save up to 25% airframe maintenance costs with the A350*. Airbus Aircraft. https://www.aircraft.airbus.com/en/newsroom/case-study/2024-10-save-up-to-25-maintenance-costs-with-the-a350

ATR 72-600. (n.d.). https://www.atr-aircraft.com/wp-content/uploads/2020/07/Factsheets_-_ATR_72-600.pdf

Barcenas, O. U. E., Pioquinto, J. G. Q., Kurkina, E., & Lukyanov, O. (2023). Surrogate aerodynamic wing modeling based on a multilayer perceptron. *Aerospace*, *10*(2), 149. https://doi.org/10.3390/aerospace10020149

Boeing Commercial Airplanes. (2024, December). 777-200LR / -300ER / -Freighter Airplane Characteristics for Airport Planning. In *Boeing*. https://www.boeing.com/content/dam/boeing/v2/airports/acaps/777-200LR-300ER-F_Rev_G.pdf

Boeing Commercial Airplanes. (2025, October). Next-Generation 737 Airplane Characteristics for airport Planning. In *Boeing*. https://www.boeing.com/content/dam/boeing/v2/airports/acaps/737NG_REV_C.pdf

Boeing Commercial Airplanes. (2026, January). 747-8 Airplane Characteristics for Airport Planning. In *Boeing*. https://www.boeing.com/content/dam/boeing/v2/airports/acaps/747-8_Rev_E.pdf

Boeing Commercial Airplanes. (n.d.). *777X*. https://www.boeing.com/commercial/777x

Caliendo, H. (2015, August 26). Battle of the composite wings. *Gardner Business Media, Inc.* https://www.compositesworld.com/articles/battle-of-the-composite-wings-

Climate Action Tracker. (2025, October). *International aviation.* https://climateactiontracker.org/sectors/aviation/

Deere, K. A., Viken, J. K., Viken, S. A., Carter, M. B., Wiese, M. R., & Farr, N. L. (2017, June 5). *Computational analysis of a wing designed for the X-57 distributed electric propulsion aircraft*. NASA Technical Reports Server (NTRS). https://ntrs.nasa.gov/citations/20170005883

Eviation. (n.d.). *Aircraft*. https://web.archive.org/web/20260304011342/https://www.eviation.com/aircraft/

Factor of safety, 14 C.F.R. § 25.303. https://www.ecfr.gov/current/title-14/section-25.303

GlobalAir.com. (n.d.). *Embraer E-175*. https://www.globalair.com/aircraft-specifications/embraer/embraer-e-175-specifications/1364

Griffin, C. F., & Harvill, W. E. (1988). *Composite transport wing technology development: Design development tests and advanced structural concepts* (NASA Contractor Report 4177). National Aeronautics and Space Administration. https://ntrs.nasa.gov/citations/19910019939

Hashin, Z. (1980, June). Failure criteria for unidirectional fiber composites. *Journal of Applied Mechanics, 47*(2), 329-334. https://doi.org/10.1115/1.3153664

International Civil Aviation Organization. (2018). Annex 14 to the Convention on International Civil Aviation: Aerodromes. Volume I: Aerodrome design and operations (8th ed.). ICAO.

Jones, D. R., Schonlau, M., & Welch, W. J. (1998). Efficient global optimization of expensive black-box functions. *Journal of Global Optimization, 13*(4), 455-492. https://doi.org/10.1023/A:1008306431147

Jones, R. M. (1999). *Mechanics of composite materials* (2nd ed.). Taylor & Francis.

Karal, M. (2001). *AST composite wing program: Executive summary* (NASA/CR-2001-210650). National Aeronautics and Space Administration, Langley Research Center. https://ntrs.nasa.gov/citations/20010033249

Korba, P., Al-Rabeei, S., Hovanec, M., Sekelová, I., & Kale, U. (2024). Structural design and material comparison for aircraft wing box beam panel. *Heliyon*, *10*(5), e27403. https://doi.org/10.1016/j.heliyon.2024.e27403

Kraft, D. (1988). *A software package for sequential quadratic programming* (DFVLR-FB 88-28). Deutsche Forschungs- und Versuchsanstalt für Luft- und Raumfahrt.

Le Clainche, S., Ferrer, E., Gibson, S., Cross, E., Parente, A., & Vinuesa, R. (2023). Improving aircraft performance using machine learning: A review. *Aerospace Science and Technology*, *138*, 108354. https://doi.org/10.1016/j.ast.2023.108354

Li, J., Du, X., & Martins, J. R. (2022). Machine learning in aerodynamic shape optimization. *Progress in Aerospace Sciences*, *134*, 100849. https://doi.org/10.1016/j.paerosci.2022.100849

Limit maneuvering load factors, 14 C.F.R. § 25.337. https://www.ecfr.gov/current/title-14/section-25.337

Megson, T. H. G. (2021). *Aircraft structures for engineering students* (6th ed.). Elsevier. https://doi.org/10.1016/C2019-0-03113-5

NASA. (2026, June 23). X-57 Maxwell Overview - NASA. *NASA*. https://www.nasa.gov/centers-and-facilities/armstrong/x-57-maxwell/

Palt, K. (n.d.). *Boeing 707 - Specifications - Technical Data / Description*. https://www.flugzeuginfo.net/acdata_php/acdata_707_en.php

Parveez, B., Kittur, M. I., Badruddin, I. A., Kamangar, S., Hussien, M., & Umarfarooq, M. A. (2022). Scientific Advancements in Composite Materials for aircraft Applications: a review. *Polymers*, *14*(22), 5007. https://doi.org/10.3390/polym14225007

Pattanayak, T., & Mavris, D. (2025). Battery technology for sustainable aviation: a review of current trends and future prospects. *Applied Energy*, *397*, 126356. https://doi.org/10.1016/j.apenergy.2025.126356

Rasmussen, C. E., & Williams, C. K. I. (2006). *Gaussian processes for machine learning.* MIT Press.

Raymer, D. P. (2018). *Aircraft design: A conceptual approach* (6th ed.). American Institute of Aeronautics and Astronautics. https://doi.org/10.2514/4.104909

Ritchie, H. (2024, April 8). *What share of global CO_2 emissions come from aviation?* Our World in Data. https://ourworldindata.org/global-aviation-emissions

Tao, J., & Sun, G. (2019). Application of deep learning based multi-fidelity surrogate model to robust aerodynamic design optimization. *Aerospace Science and Technology*, *92*, 722–737. https://doi.org/10.1016/j.ast.2019.07.002

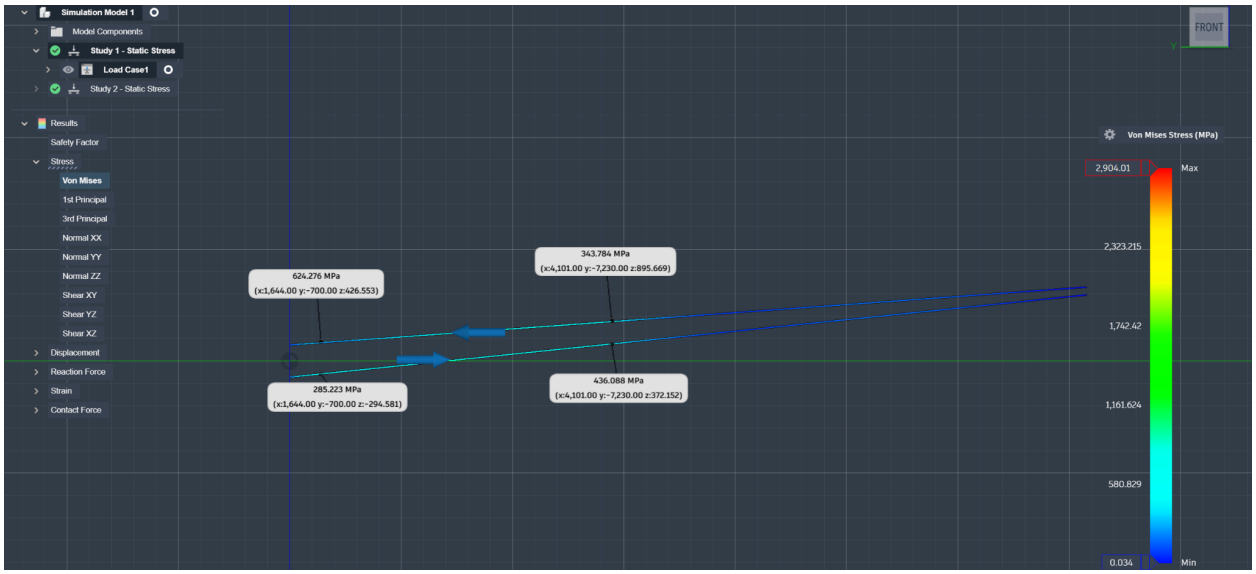
Tsai, S. W., & Wu, E. M. (1971). A general theory of strength for anisotropic materials. *Journal of Composite Materials, 5*(1), 58-80. https://doi.org/10.1177/002199837100500106

APPENDIX

Figures 18-45 show the von Mises stress contours for the remaining cases not shown above (A320-200 CFRP Baseline and ML-Optimized CFRP and all other aircraft cases), each having their probe values listed in Table 5. Figures 16-17 are in the main text.

Figure 18

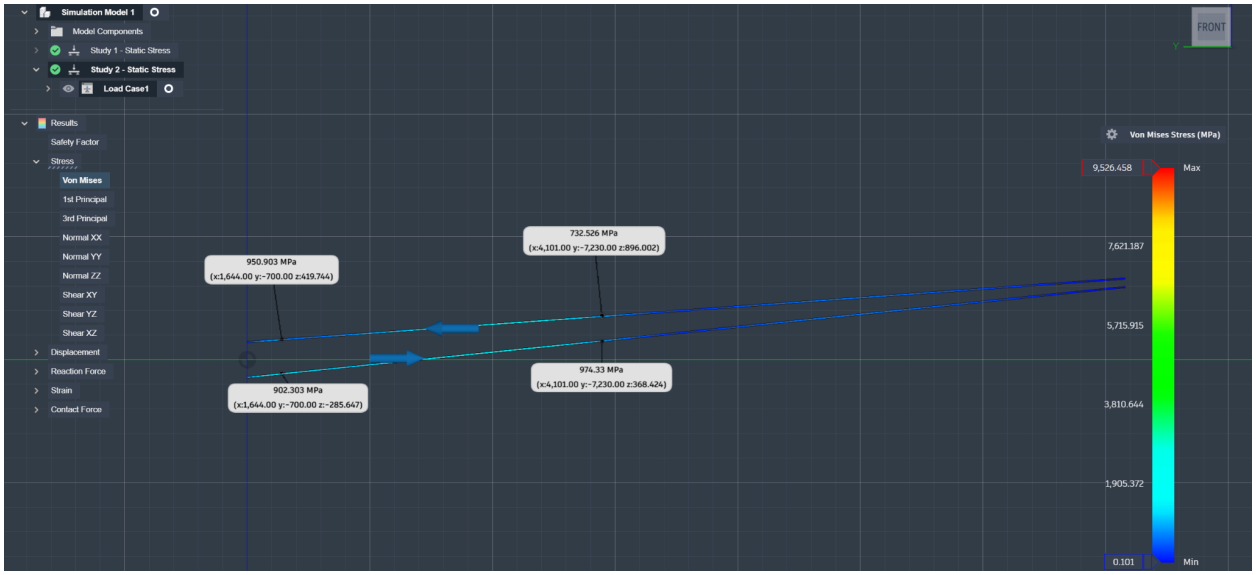
A320-200 Wing Spar (CFRP Baseline) – von Mises Stress, Cruise (1g) Load Case



Note. Autodesk Fusion 360 static stress study, von Mises stress distribution for the A320-200 spar-cap model (CFRP Baseline) under the cruise (1g) load case. Reported global maximum stress: 2,904.0 MPa.

Figure 19

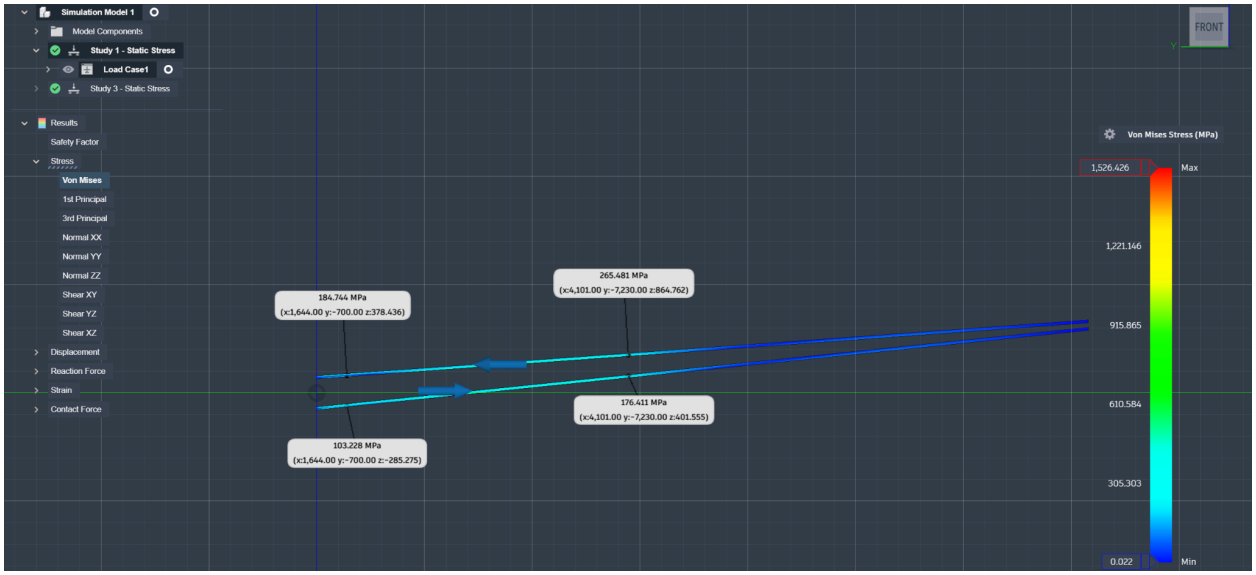
A320-200 Wing Spar (CFRP Baseline) – von Mises Stress, Ultimate (3.75g) Load Case



Note. Autodesk Fusion 360 static stress study, von Mises stress distribution for the A320-200 spar-cap model (CFRP Baseline) under the Ultimate (3.75g) load case. Reported global maximum stress: 9,526.5 MPa.

Figure 20

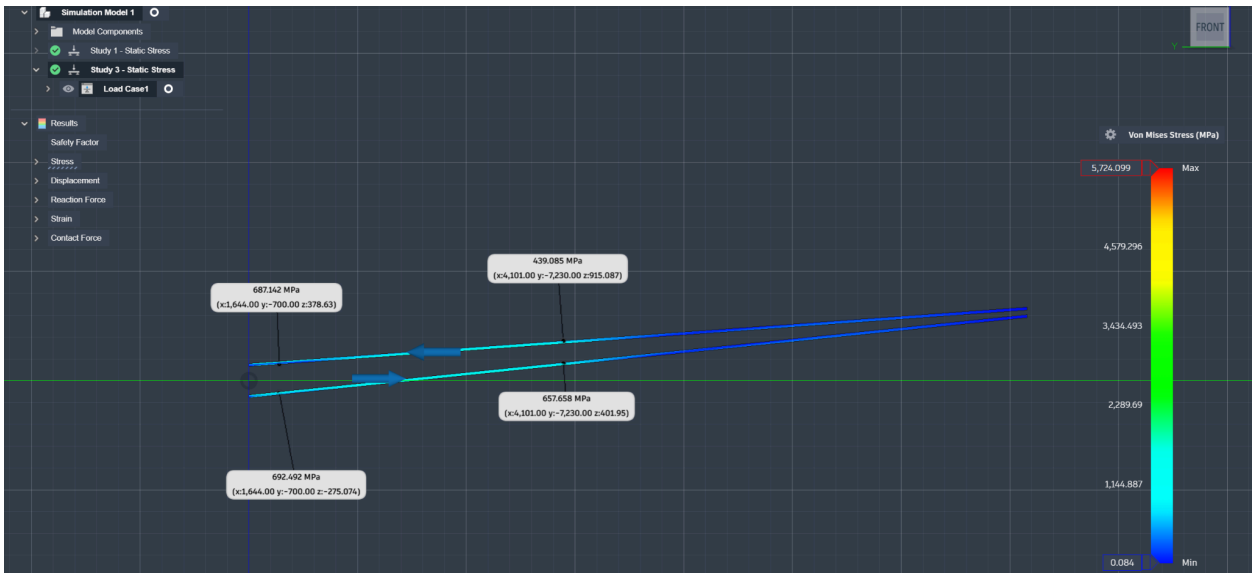
A320-200 Wing Spar (ML-Optimized CFRP) – von Mises Stress, Cruise (1g) Load Case



Note. Autodesk Fusion 360 static stress study, von Mises stress distribution for the A320-200 spar-cap model (ML-Optimized CFRP) under the cruise (1g) load case. Reported global maximum stress: 1,526.4 MPa.

Figure 21

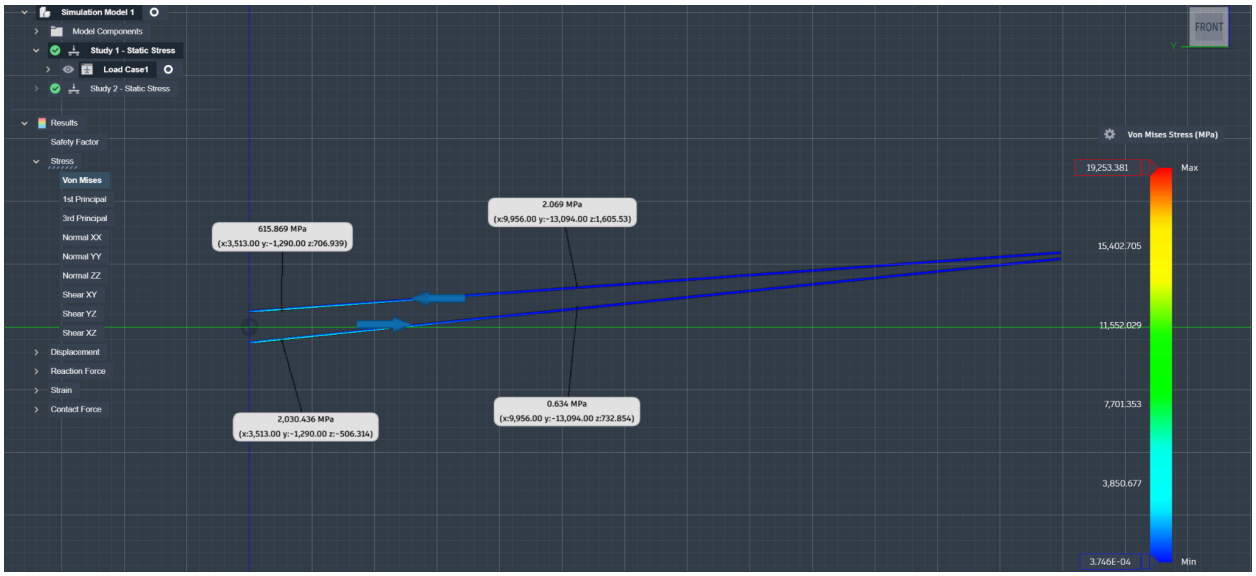
A320-200 Wing Spar (ML-Optimized CFRP) – von Mises Stress, Ultimate (3.75g) Load Case



Note. Autodesk Fusion 360 static stress study, von Mises stress distribution for the A320-200 spar-cap model (ML-Optimized CFRP) under the Ultimate (3.75g) load case. Reported global maximum stress: 5724.1 MPa.

Figure 22

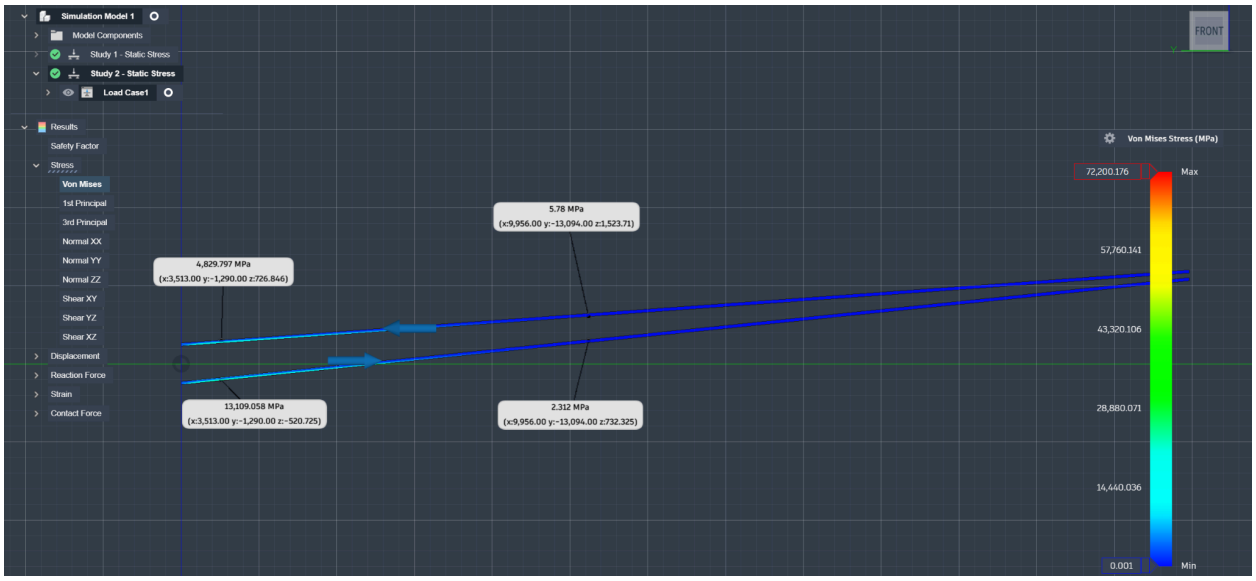
Boeing 777-300ER Wing Spar (Aluminum 7075-T6) – von Mises Stress, Cruise (1g) Load Case



Note. Autodesk Fusion 360 static stress study, von Mises stress distribution for the Boeing 777-300ER spar-cap model (Aluminum 7075-T6) for the Cruise (1g) load case. Reported global maximum stress: 19,253.4 MPa (cap force F).

Figure 23

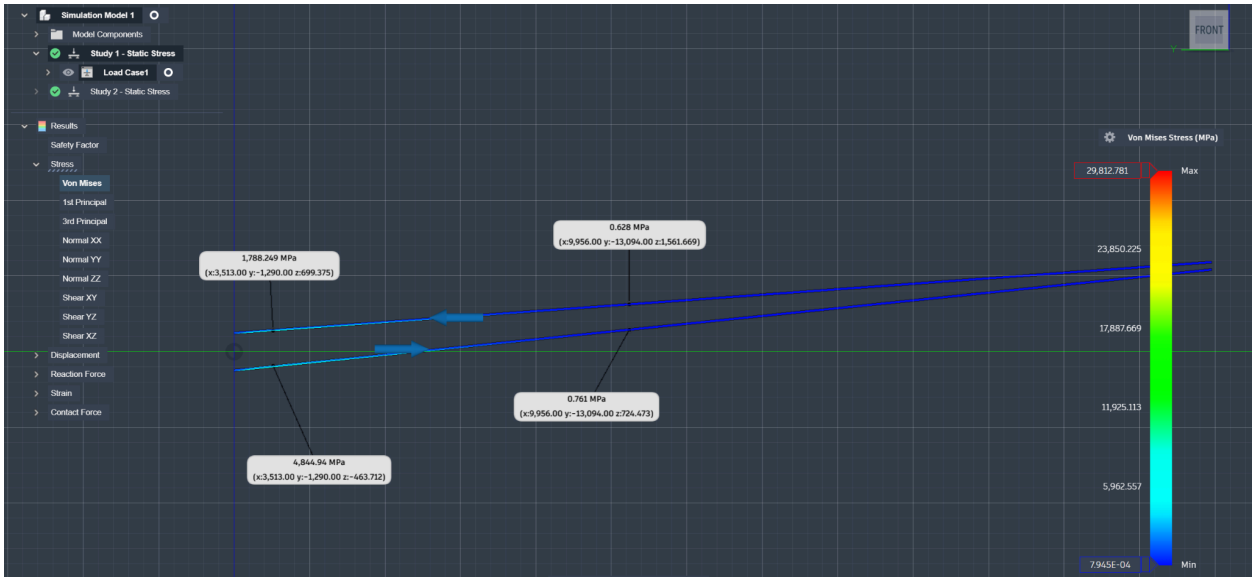
Boeing 777-300ER Wing Spar (Aluminum 7075-T6) – von Mises Stress, Ultimate (3.75g) Load



Note. Autodesk Fusion 360 static stress study, von Mises stress distribution for the Boeing 777-300ER spar-cap model (Aluminum 7075-T6) for the Ultimate (3.75g) load case. Reported global maximum stress: 72,200.2 MPa (cap force F).

Figure 24

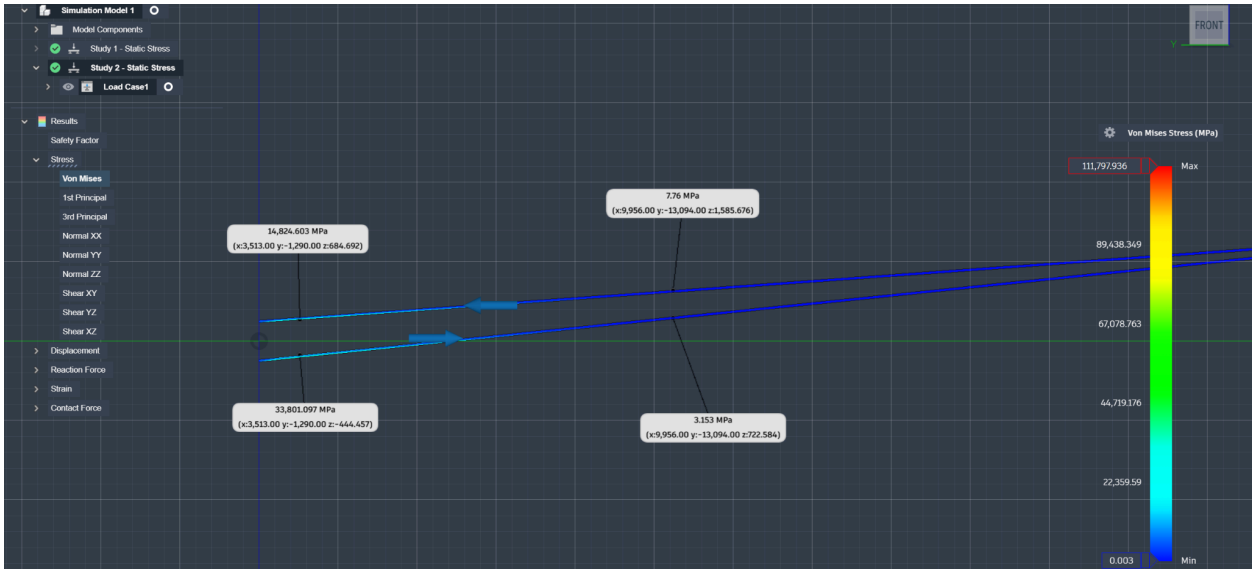
Boeing 777-300ER Wing Spar (CFRP Baseline) – von Mises Stress, Cruise (1g) Load Case



Note. Autodesk Fusion 360 static stress study, von Mises stress distribution for the Boeing 777-300ER spar-cap model (CFRP Baseline) for the Cruise (1g) load case. Reported global maximum stress: 29,812.8 MPa (cap force F).

Figure 25

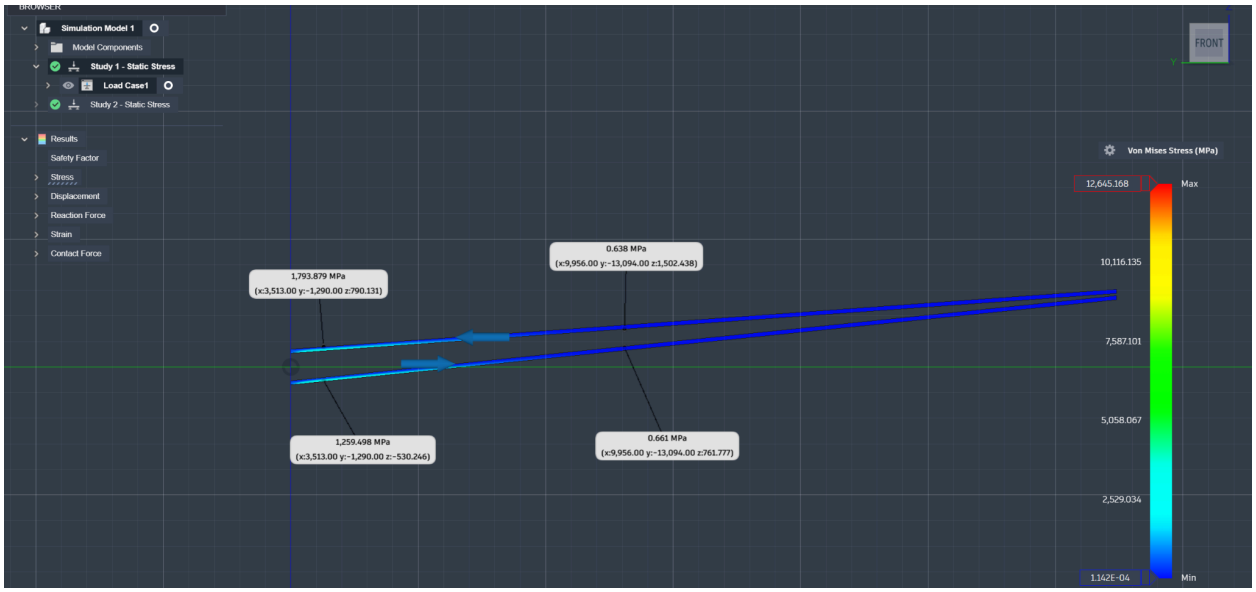
Boeing 777-300ER Wing Spar (CFRP Baseline) – von Mises Stress, Ultimate (3.75g) Load



Note. Autodesk Fusion 360 static stress study, von Mises stress distribution for the Boeing 777-300ER spar-cap model (CFRP Baseline) for the Ultimate (3.75g) load case. Reported global maximum stress: 111,797.9 MPa (cap force F).

Figure 26

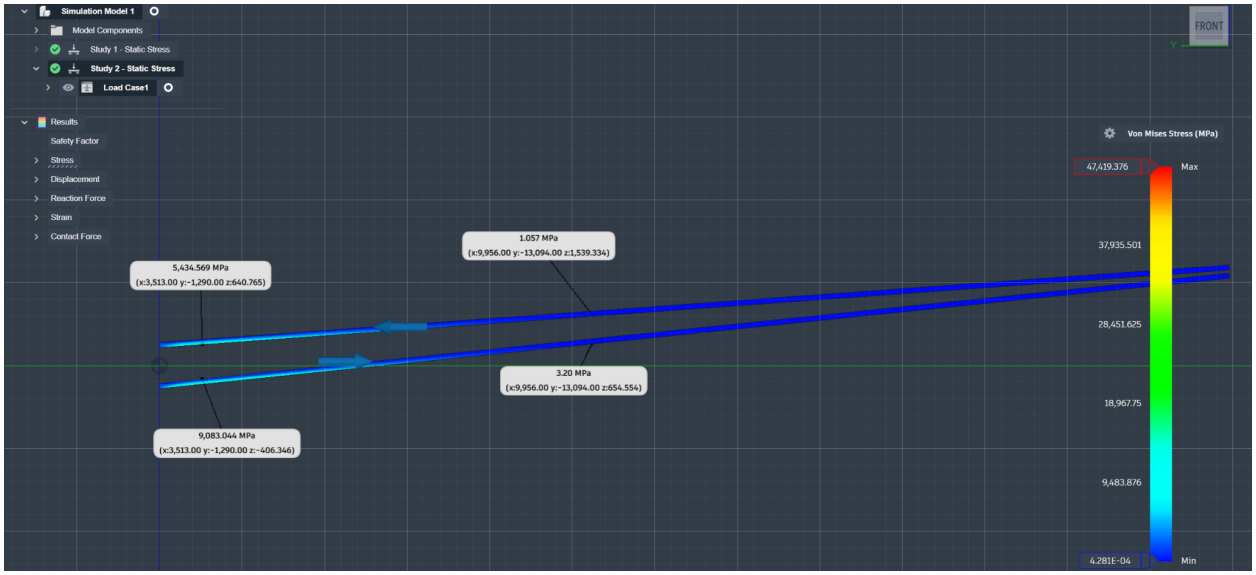
Boeing 777-300ER Wing Spar (ML-Optimized CFRP) – von Mises Stress, Cruise (1g) Load



Note. Autodesk Fusion 360 static stress study, von Mises stress distribution for the Boeing 777-300ER spar-cap model (ML-Optimized CFRP) for the Cruise (1g) load case. Reported global maximum stress: 12,645.2 MPa (cap force F).

Figure 27

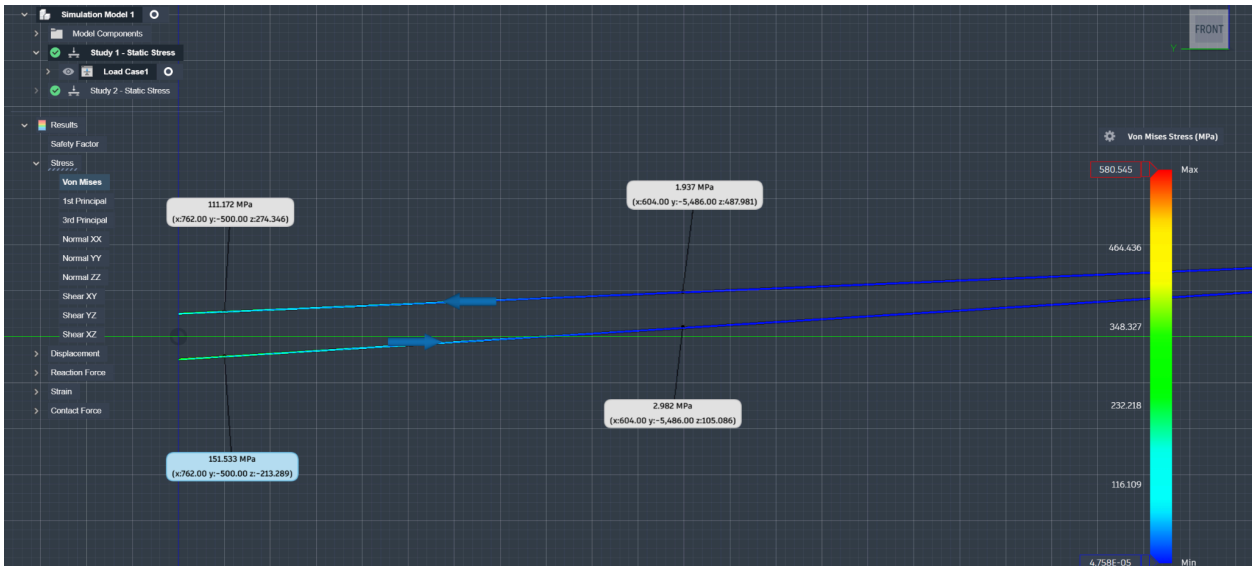
Boeing 777-300ER Wing Spar (ML-Optimized CFRP) – von Mises Stress, Ultimate (3.75g) Load



Note. Autodesk Fusion 360 static stress study, von Mises stress distribution for the Boeing 777-300ER spar-cap model (ML-Optimized CFRP) for the Ultimate (3.75g) load case. Reported global maximum stress: 47,419.4 MPa (cap force F).

Figure 28

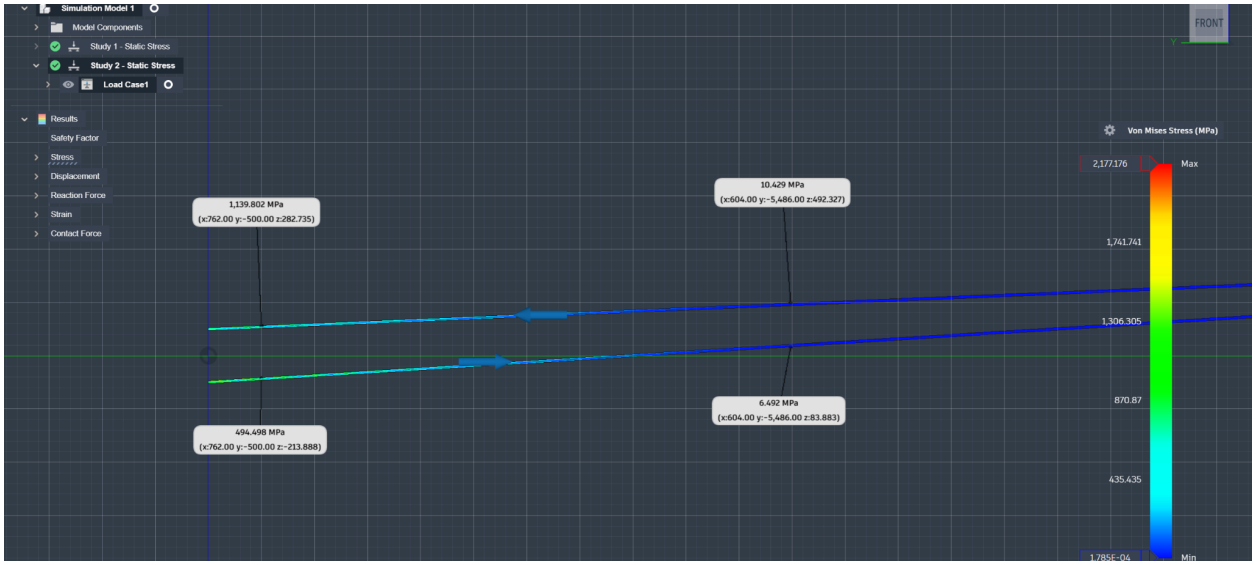
ATR 72-600 Wing Spar (Aluminum 7075-T6) – von Mises Stress, Cruise (1g) Load Case



Note. Autodesk Fusion 360 static stress study, von Mises stress distribution for the ATR 72-600 spar-cap model (Aluminum 7075-T6) for the Cruise (1g) load case. Global maximum stress shown: 580.5 MPa (solved at the transverse force P); scaled to the cap force F: 6,689.0 MPa.

Figure 29

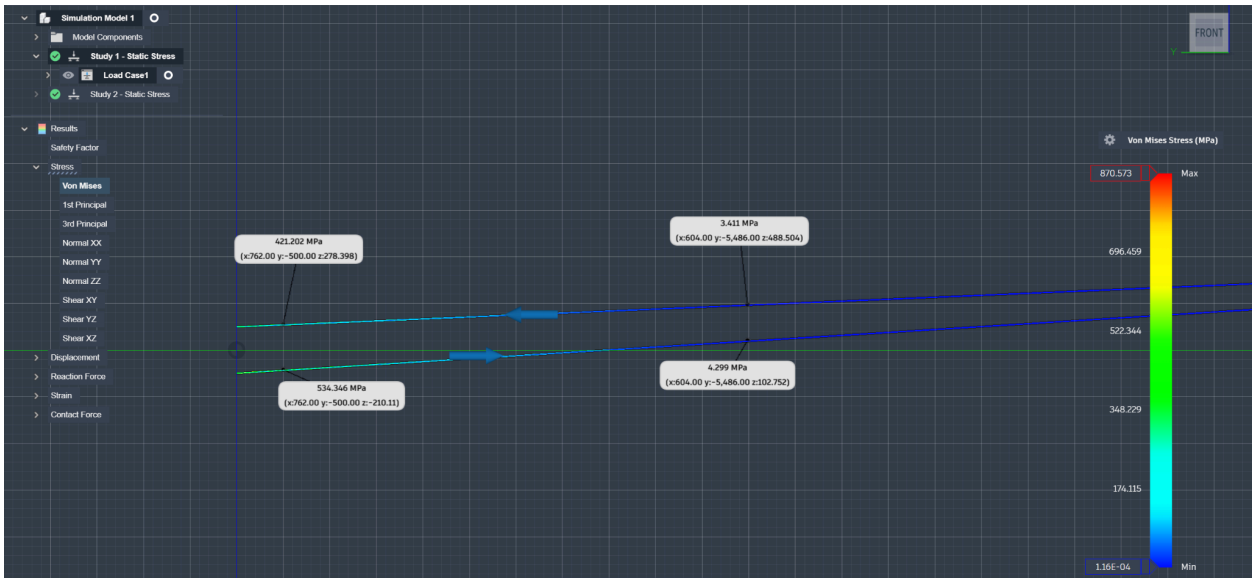
ATR 72-600 Wing Spar (Aluminum 7075-T6) – von Mises Stress, Ultimate (3.75g) Load Case



Note. Autodesk Fusion 360 static stress study, von Mises stress distribution for the ATR 72-600 spar-cap model (Aluminum 7075-T6) for the Ultimate (3.75g) load case. Global maximum stress shown: 2,177.2 MPa (solved at the transverse force P); scaled to the cap force F: 25,087.4 MPa.

Figure 30

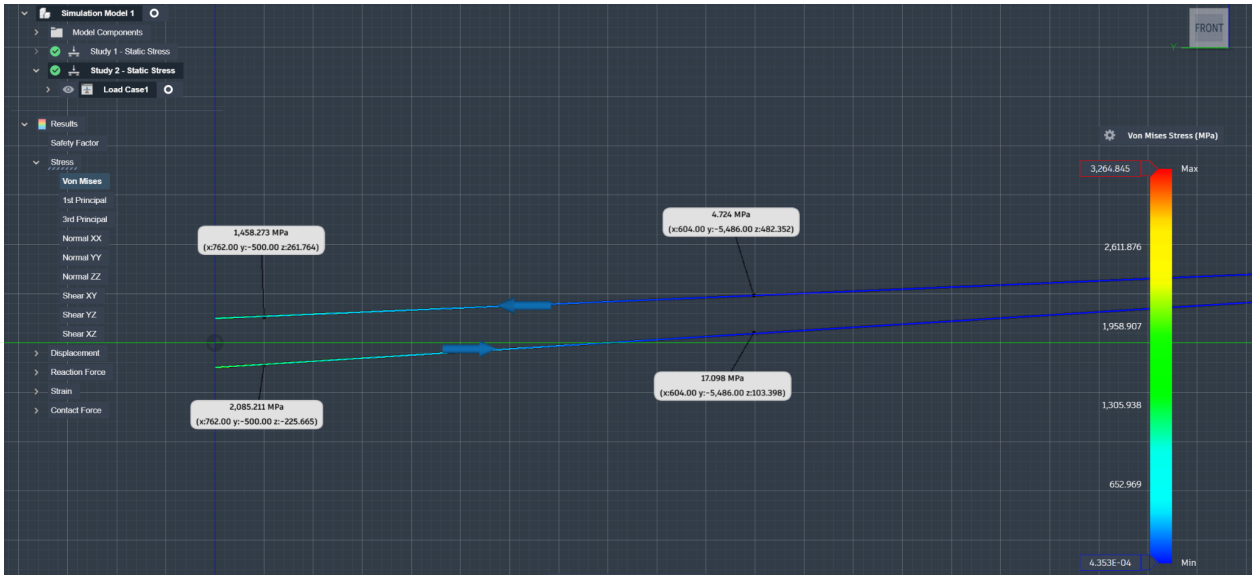
ATR 72-600 Wing Spar (CFRP Baseline) – von Mises Stress, Cruise (1g) Load Case



Note. Autodesk Fusion 360 static stress study, von Mises stress distribution for the ATR 72-600 spar-cap model (CFRP Baseline) for the Cruise (1g) load case. Global maximum stress shown: 870.6 MPa (solved at the transverse force P); scaled to the cap force F: 10,031.7 MPa.

Figure 31

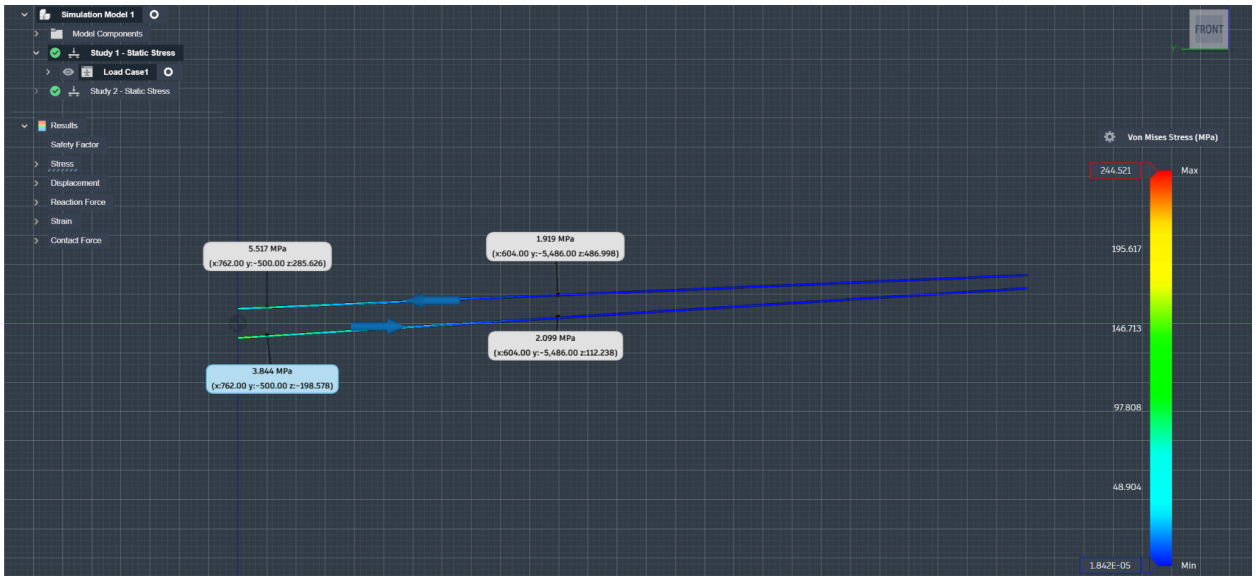
ATR 72-600 Wing Spar (CFRP Baseline) – von Mises Stress, Ultimate (3.75g) Load Case



Note. Autodesk Fusion 360 static stress study, von Mises stress distribution for the ATR 72-600 spar-cap model (CFRP Baseline) for the Ultimate (3.75g) load case. Global maximum stress shown: 3,264.8 MPa (solved at the transverse force P); scaled to the cap force F: 37,619.6 MPa.

Figure 32

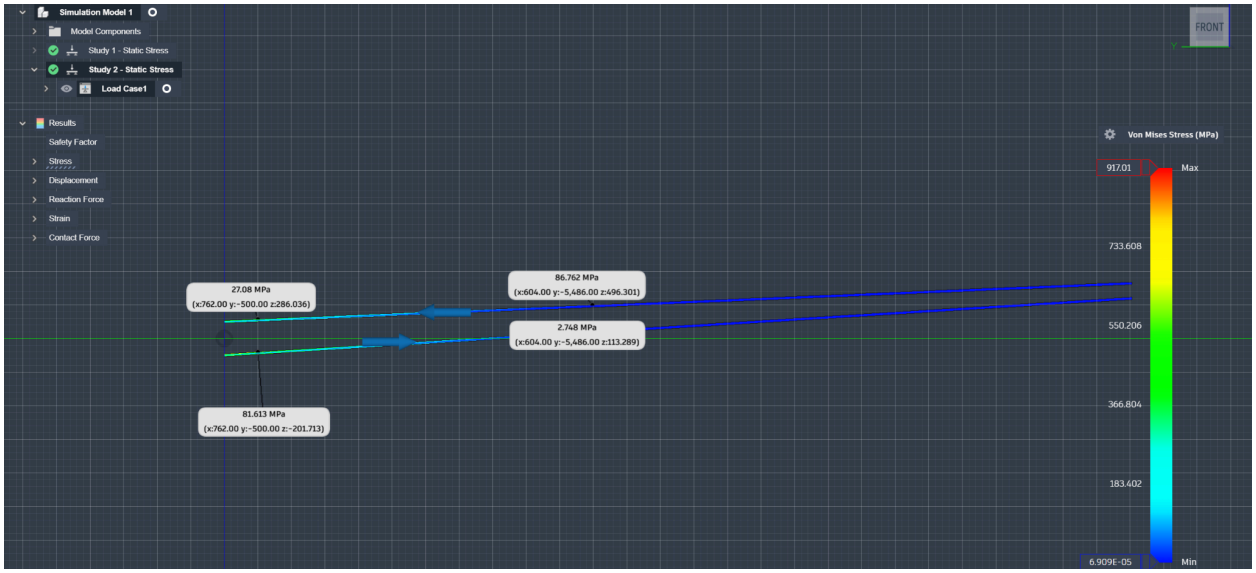
ATR 72-600 Wing Spar (ML-Optimized CFRP) – von Mises Stress, Cruise (1g) Load Case



Note. Autodesk Fusion 360 static stress study, von Mises stress distribution for the ATR 72-600 spar-cap model (ML-Optimized CFRP) for the Cruise (1g) load case. Global maximum stress shown: 244.5 MPa (solved at the transverse force P); scaled to the cap force F: 2,817.3 MPa.

Figure 33

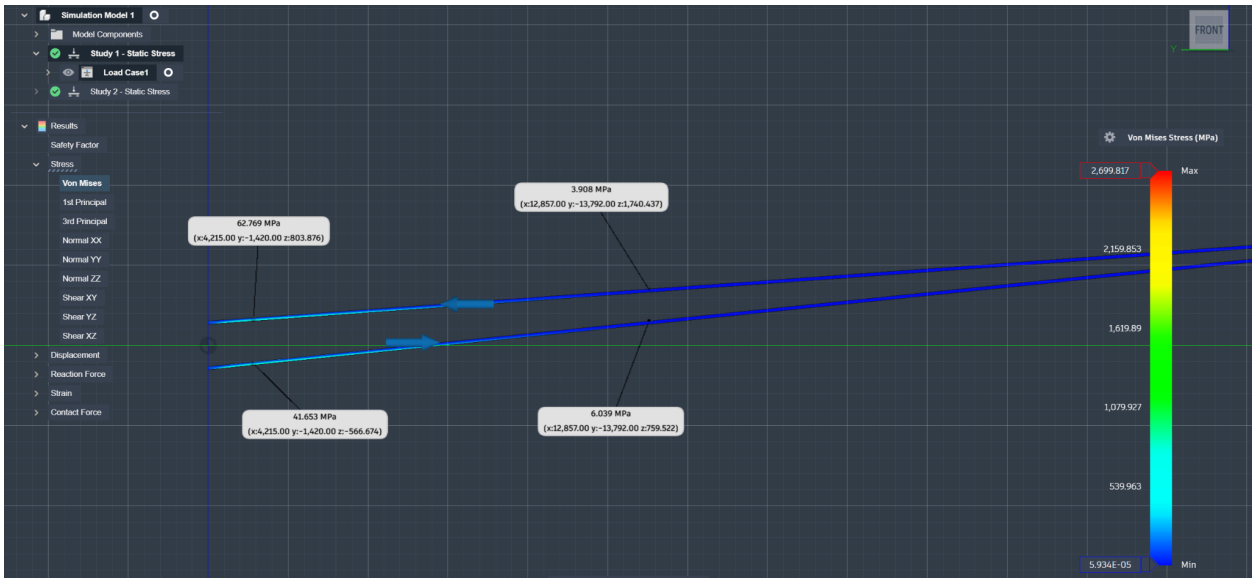
ATR 72-600 Wing Spar (ML-Optimized CFRP) – von Mises Stress, Ultimate (3.75g) Load Case



Note. Autodesk Fusion 360 static stress study, von Mises stress distribution for the ATR 72-600 spar-cap model (ML-Optimized CFRP) for the Ultimate (3.75g) load case. Global maximum stress shown: 917.0 MPa (solved at the transverse force P); scaled to the cap force F: 10,566.4 MPa.

Figure 34

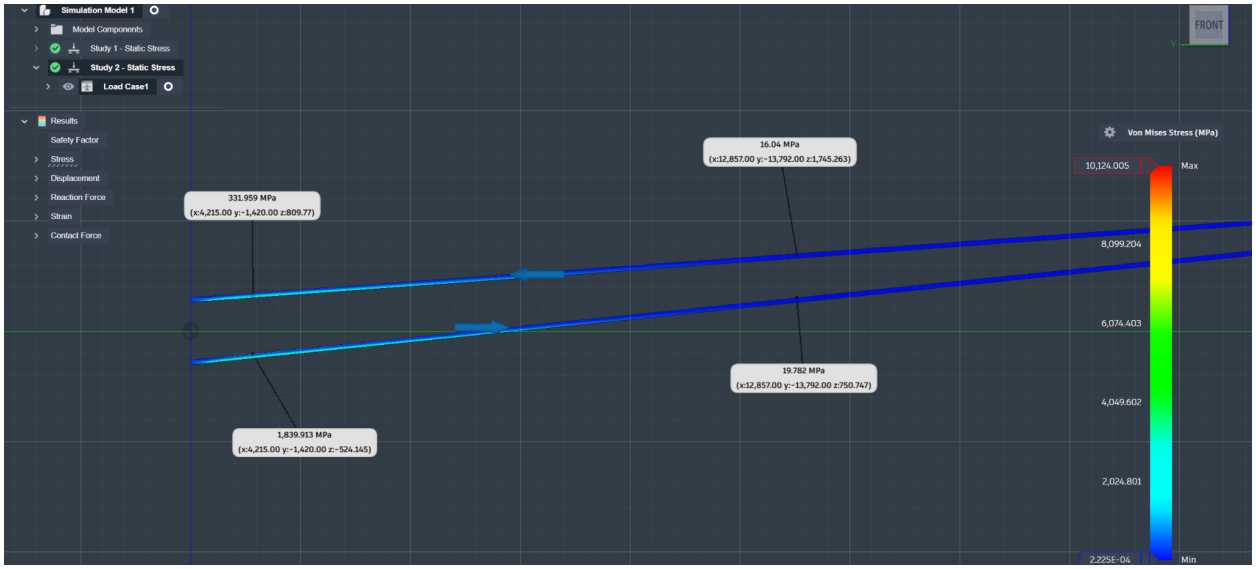
Boeing 747-8F Wing Spar (Aluminum 7075-T6) – von Mises Stress, Cruise (1g) Load Case



Note. Autodesk Fusion 360 static stress study, von Mises stress distribution for the Boeing 747-8F spar-cap model (Aluminum 7075-T6) for the Cruise (1g) load case. Global maximum stress shown: 2,699.8 MPa (solved at the transverse force P); scaled to the cap force F: 27,604.1 MPa.

Figure 35

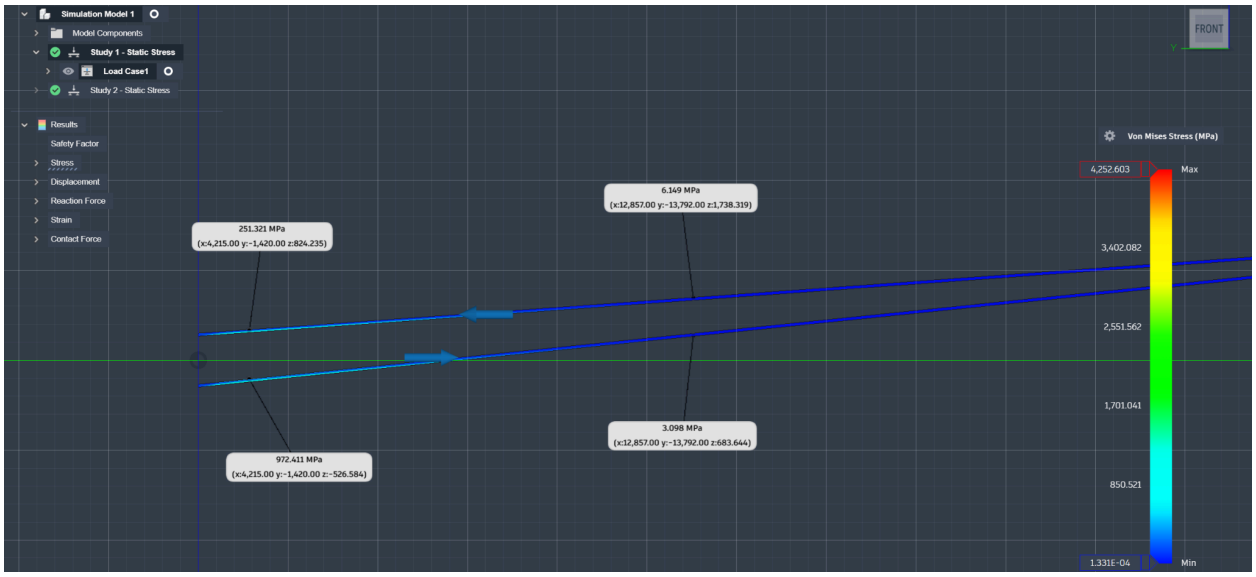
Boeing 747-8F Wing Spar (Aluminum 7075-T6) – von Mises Stress, Ultimate (3.75g) Load Case



Note. Autodesk Fusion 360 static stress study, von Mises stress distribution for the Boeing 747-8F spar-cap model (Aluminum 7075-T6) for the Ultimate (3.75g) load case. Global maximum stress shown: 10,124.0 MPa (solved at the transverse force P); scaled to the cap force F: 103,512.8 MPa.

Figure 36

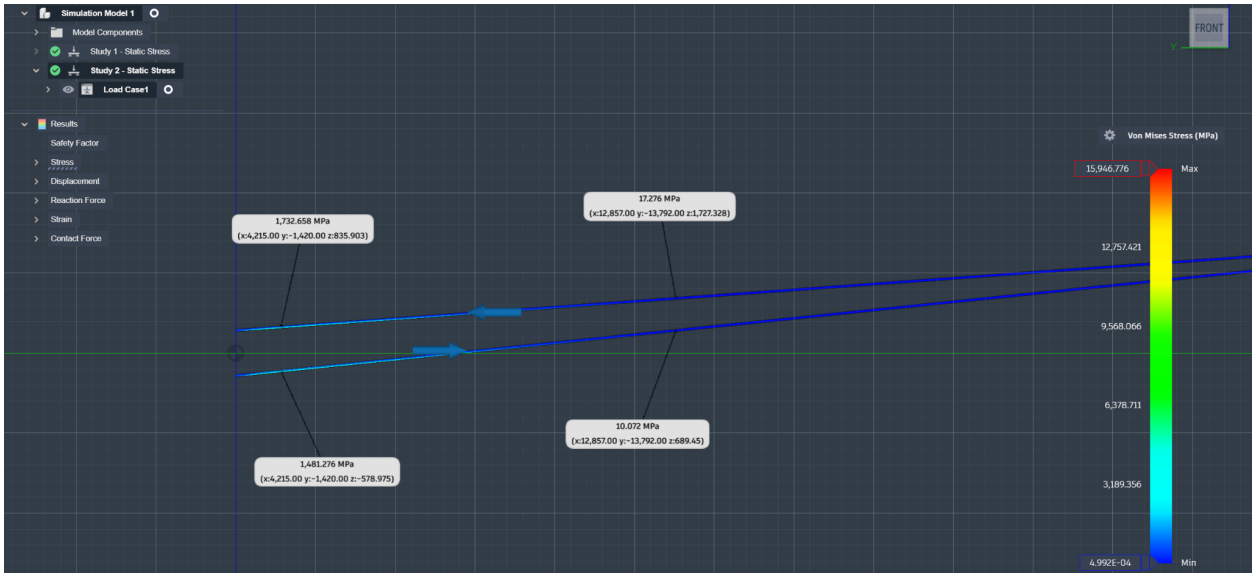
Boeing 747-8F Wing Spar (CFRP Baseline) – von Mises Stress, Cruise (1g) Load Case



Note. Autodesk Fusion 360 static stress study, von Mises stress distribution for the Boeing 747-8F spar-cap model (CFRP Baseline) for the Cruise (1g) load case. Global maximum stress shown: 4,252.6 MPa (solved at the transverse force P); scaled to the cap force F: 43,480.7 MPa.

Figure 37

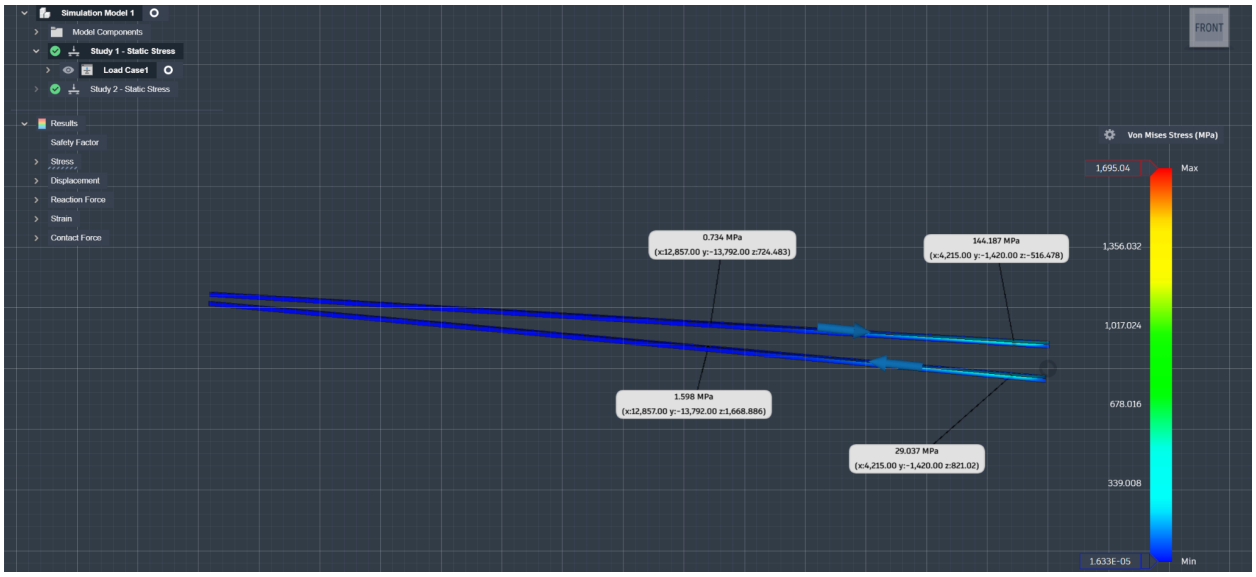
Boeing 747-8F Wing Spar (CFRP Baseline) – von Mises Stress, Ultimate (3.75g) Load Case



Note. Autodesk Fusion 360 static stress study, von Mises stress distribution for the Boeing 747-8F spar-cap model (CFRP Baseline) for the Ultimate (3.75g) load case. Global maximum stress shown: 15,946.8 MPa (solved at the transverse force P); scaled to the cap force F: 163,048.1 MPa.

Figure 38

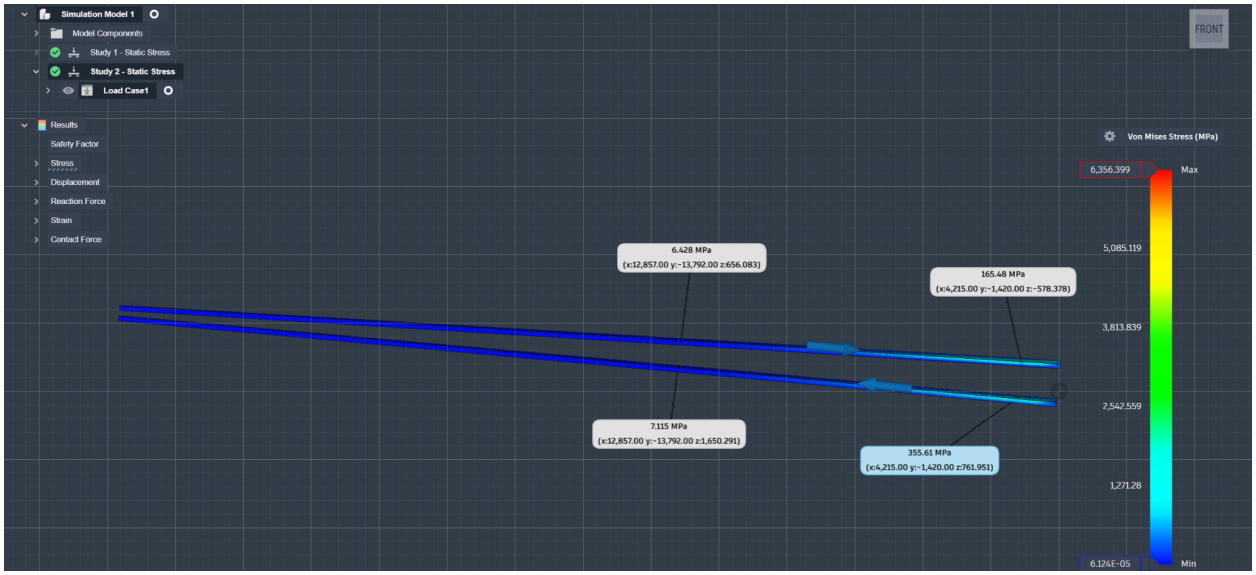
Boeing 747-8F Wing Spar (ML-Optimized CFRP) – von Mises Stress, Cruise (1g) Load Case



Note. Autodesk Fusion 360 static stress study, von Mises stress distribution for the Boeing 747-8F spar-cap model (ML-Optimized CFRP) for the Cruise (1g) load case. Global maximum stress shown: 1,695.0 MPa (solved at the transverse force P); scaled to the cap force F: 17,330.5 MPa.

Figure 39

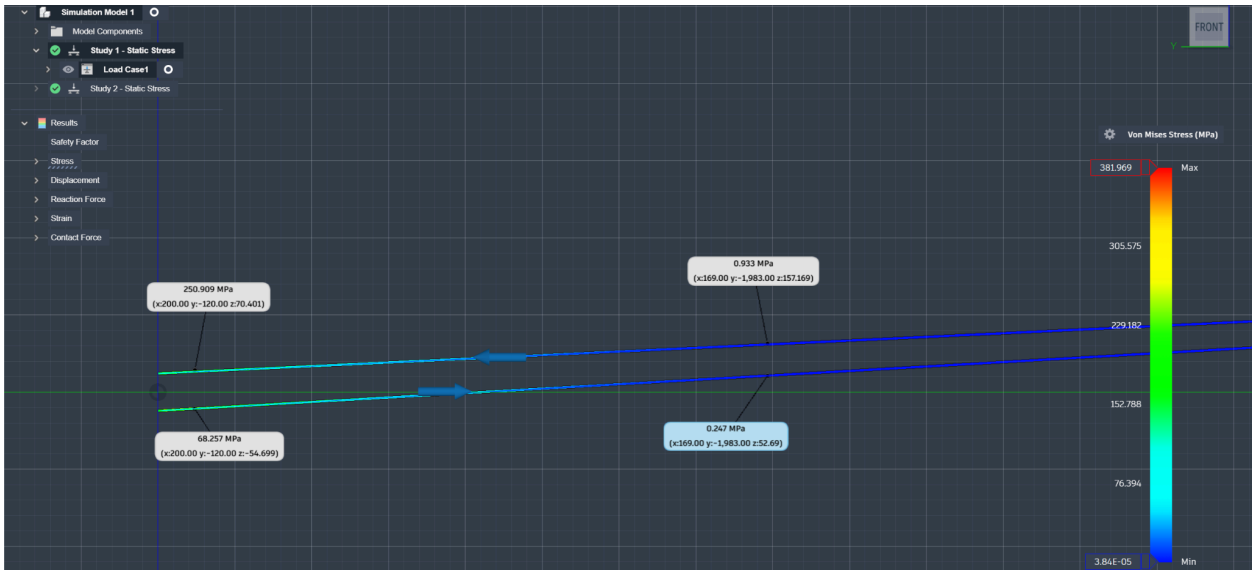
Boeing 747-8F Wing Spar (ML-Optimized CFRP) – von Mises Stress, Ultimate (3.75g) Load Case



Note. Autodesk Fusion 360 static stress study, von Mises stress distribution for the Boeing 747-8F spar-cap model (ML-Optimized CFRP) for the Ultimate (3.75g) load case. Global maximum stress shown: 6,356.4 MPa (solved at the transverse force P); scaled to the cap force F: 64,991.0 MPa.

Figure 40

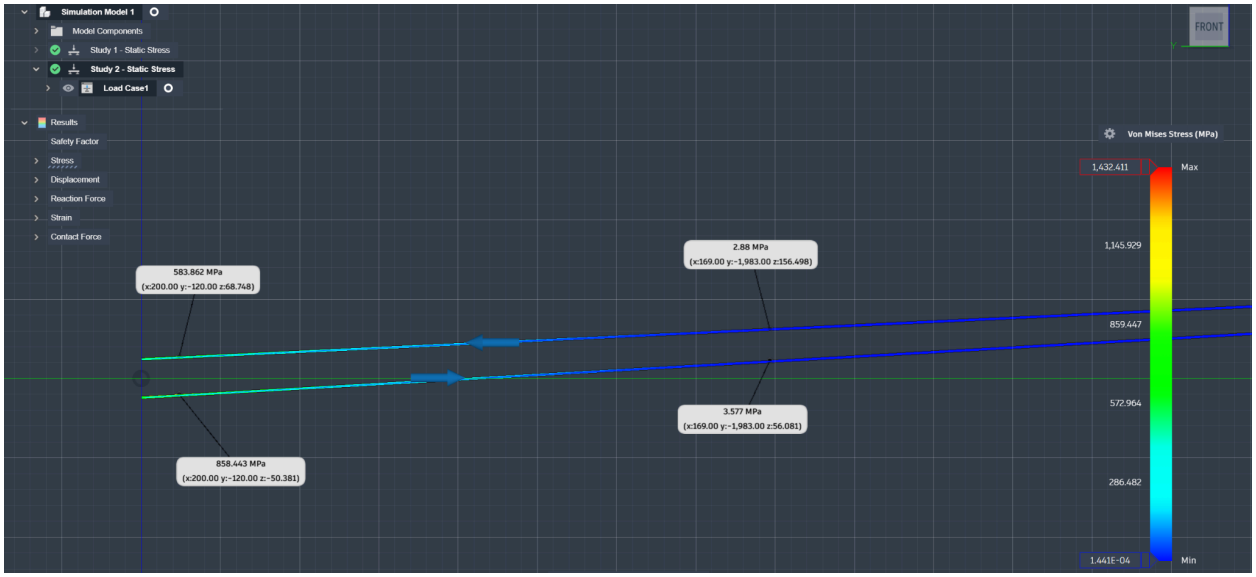
NASA X-57 Maxwell Wing Spar (Aluminum 7075-T6) – von Mises Stress, Cruise (1g) Load Case



Note. Autodesk Fusion 360 static stress study, von Mises stress distribution for the NASA X-57 Maxwell spar-cap model (Aluminum 7075-T6) for the Cruise (1g) load case. Global maximum stress shown: 382.0 MPa (solved at the transverse force P); scaled to the cap force F: 6,453.1 MPa.

Figure 41

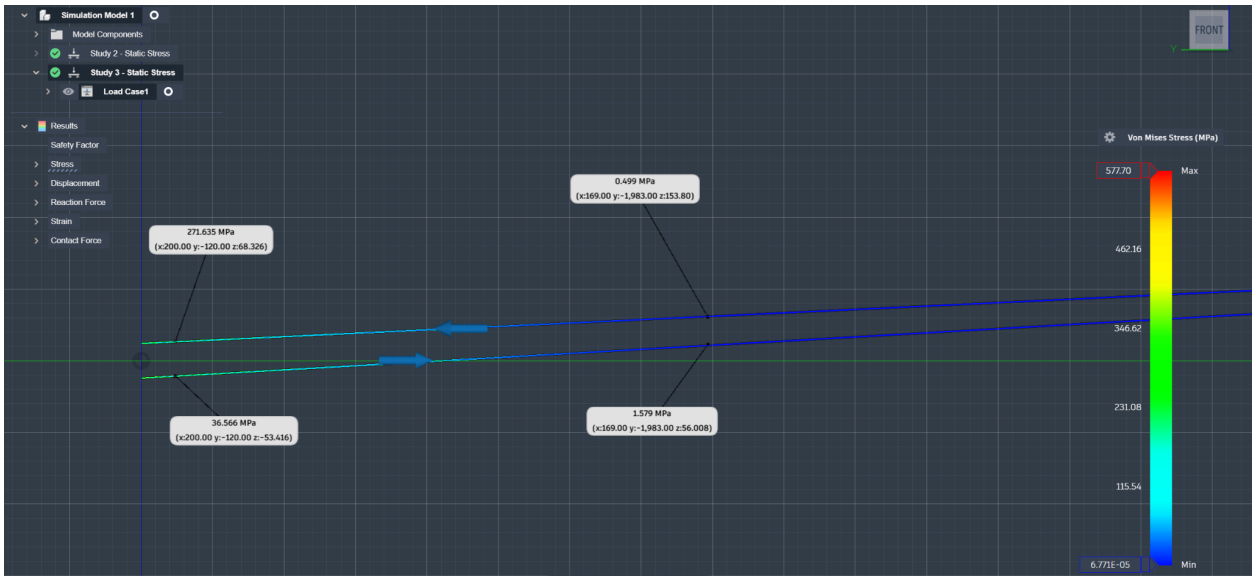
NASA X-57 Maxwell Wing Spar (Aluminum 7075-T6) – von Mises Stress, Ultimate (3.75g) Load Case



Note. Autodesk Fusion 360 static stress study, von Mises stress distribution for the NASA X-57 Maxwell spar-cap model (Aluminum 7075-T6) for the Ultimate (3.75g) load case. Global maximum stress shown: 1,432.4 MPa (solved at the transverse force P); scaled to the cap force F: 24,197.4 MPa.

Figure 42

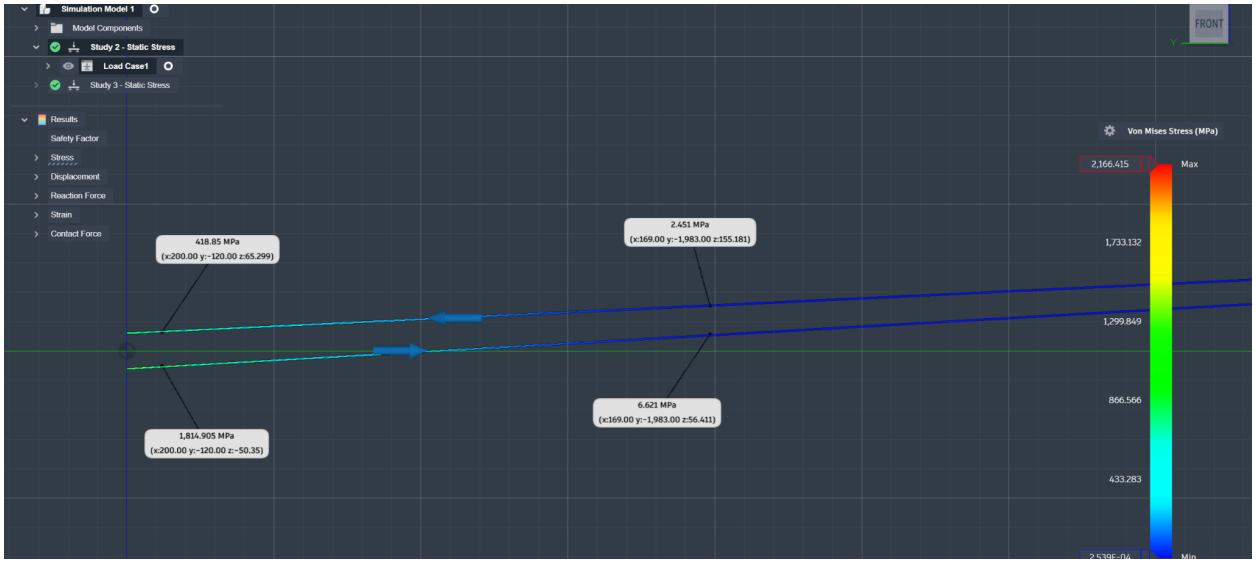
NASA X-57 Maxwell Wing Spar (CFRP Baseline) – von Mises Stress, Cruise (1g) Load Case



Note. Autodesk Fusion 360 static stress study, von Mises stress distribution for the NASA X-57 Maxwell spar-cap model (CFRP Baseline) for the Cruise (1g) load case. Global maximum stress shown: 577.7 MPa (solved at the transverse force P); scaled to the cap force F: 9,759.0 MPa.

Figure 43

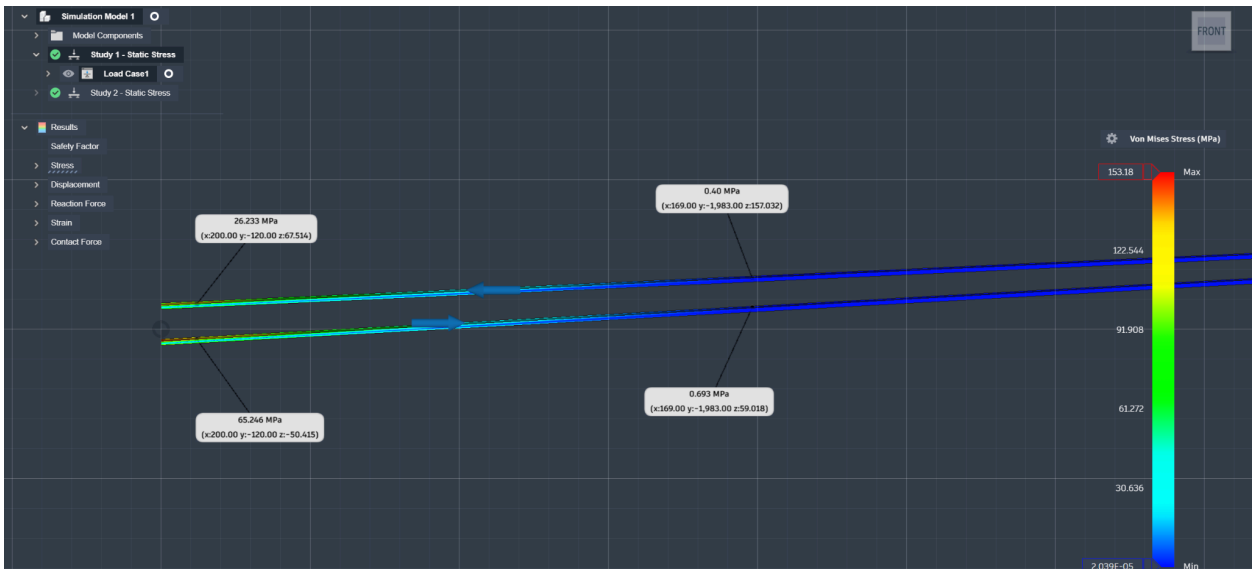
NASA X-57 Maxwell Wing Spar (CFRP Baseline) – von Mises Stress, Ultimate (3.75g) Load Case



Note. Autodesk Fusion 360 static stress study, von Mises stress distribution for the NASA X-57 Maxwell spar-cap model (CFRP Baseline) for the Ultimate (3.75g) load case. Global maximum stress shown: 2,166.4 MPa (solved at the transverse force P); scaled to the cap force F: 36,596.8 MPa.

Figure 44

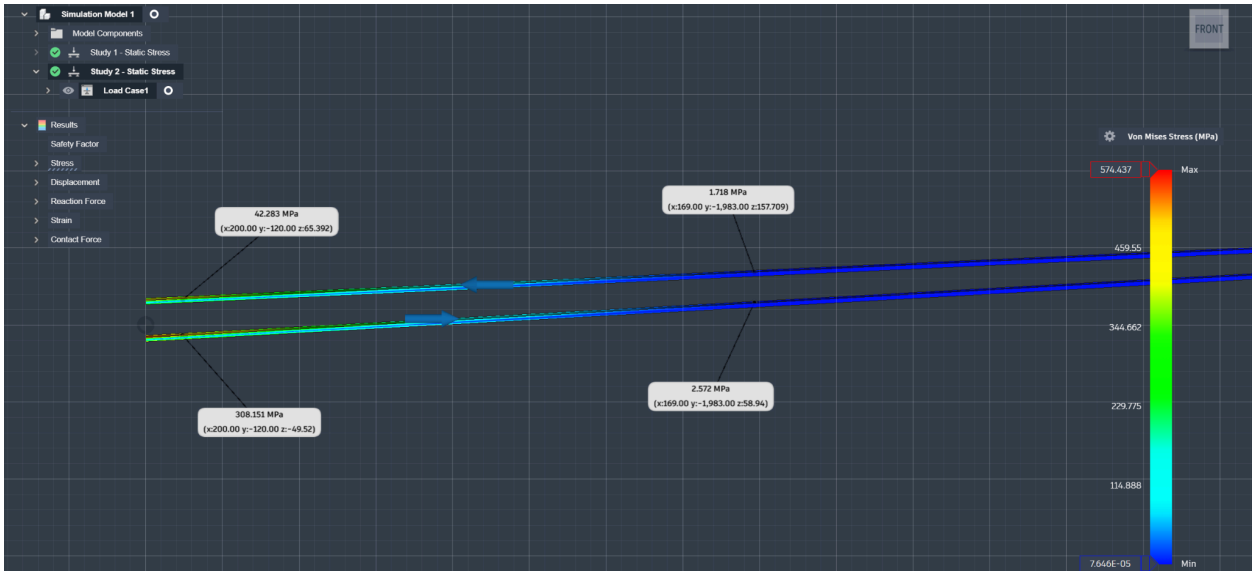
NASA X-57 Maxwell Wing Spar (ML-Optimized CFRP) – von Mises Stress, Cruise (1g) Load Case



Note. Autodesk Fusion 360 static stress study, von Mises stress distribution for the NASA X-57 Maxwell spar-cap model (ML-Optimized CFRP) for the Cruise (1g) load case. Global maximum stress shown: 153.2 MPa (solved at the transverse force P); scaled to the cap force F: 2,588.0 MPa.

Figure 45

NASA X-57 Maxwell Wing Spar (ML-Optimized CFRP) – von Mises Stress, Ultimate (3.75g) Load Case



Note. Autodesk Fusion 360 static stress study, von Mises stress distribution for the NASA X-57 Maxwell spar-cap model (ML-Optimized CFRP) for the Ultimate (3.75g) load case. Global maximum stress shown: 574.4 MPa (solved at the transverse force P); scaled to the cap force F: 9,703.3 MPa.